JAAS

PAPER

View Article Online
View Journal | View Issue

Cite this: *J. Anal. At. Spectrom.*, 2025, **40**, 3192

LA-ICP-TOF-MS for quantitative mapping of biogenic carbonate samples using matrix-matched nanoparticulate pressed powder pellets

Ana Lores-Padin, *[a] Thibaut Van Acker, [a] Niels J. de Winter,[b] Martin Wiech, [c] Simon Nordstad,[d] Yannic Hallier[d] and Frank Vanhaecke [a]

This study evaluated the micro-homogeneity of seven different commercially available nanoparticulate pressed pellets based on a $CaCO_3$ matrix and their utility for quantitative elemental mapping of biogenic carbonates using laser ablation-inductively coupled plasma-time-of-flight-mass spectrometry (LA-ICP-TOF-MS). The analytical performance of matrix-matched calibration (using the aforementioned nano-pellets) was compared against that of non-matrix-matched calibration using a silicate glass (NIST SRM 610) reference material for quantification. Calibration with nano-pellets, combined with the use of Ca as an internal standard, significantly improved the quantification accuracy, providing recoveries between 80–120% for the majority of the 18 elements selected and spread across a wide concentration range (from sub-μg g^{-1} to tens of wt%). However, some nano-pellets (*e.g.*, BPLM-NP and BAM-RS3-NP) exhibited higher heterogeneity, leading to biased recoveries. Also, an inverse correlation between the mass fraction and the relative standard deviation (RSD) was observed. Throughout the work, elemental mapping was conducted with a laser beam size of 20 × 20 μm^2 as a compromise between spatial resolution, sensitivity (sub-μg g^{-1} limits of detection required for trace elements), linear dynamic range, total analysis time and size of the region-of-interest. The quantitative mapping approach enabled the generation of high-resolution, multi-elemental 2D-maps of various $CaCO_3$-based natural chronological archives, including fish otoliths and bivalve shells, revealing detailed elemental distribution patterns for both trace (*e.g.*, Mn, Ba) and major elements (*e.g.*, Sr). This LA-ICP-TOF-MS methodology provides

Received 18th July 2025
Accepted 9th September 2025

DOI: 10.1039/d5ja00280j

rsc.li/jaas

[a]*Atomic & Mass Spectrometry-A&MS Research Group, Department of Chemistry, Ghent University, Campus Sterre, Krijgslaan 281-S12, 9000 Ghent, Belgium. E-mail: ana.lorespadin@ugent.be*

[b]*Departement of Earth Sciences, Vrije Universiteit Amsterdam, W&N Building, De Boelelaan 1085, 1081 Amsterdam, the Netherlands*

[c]*Departement of Foreign and Infectious Substances, Institute of Marine Research, P. O. Box 1870, Nordnes, NO-5817 Bergen, Norway*

[d]*myStandards GmbH, Schauenburger Straße 116, 24118 Kiel, Germany*

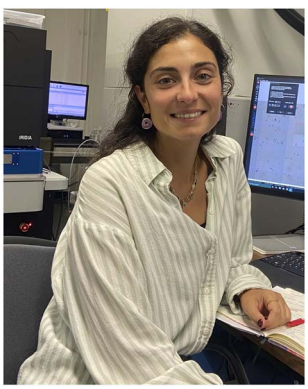

Ana Lores-Padin

Dr Ana Lores Padín is a Junior Postdoctoral Fellow (FWO) in the Atomic and Mass Spectrometry (A&MS) Research Group at Ghent University, led by Prof. Frank Vanhaecke. She obtained her PhD in Analytical Chemistry cum laude in 2022 from the University of Oviedo (Spain), under the supervision of Prof. Rosario Pereiro and Dr Beatriz Fernandez. Her doctoral research focused on developing innovative analytical methods based on metal tags and laser ablation (LA) and single-cell (SC) ICP-MS for the detection of neurodegenerative disease-related proteins. During her PhD, she also completed a research stay at the University of Crete (Greece) with Prof. Spiros Pergantis, where she began exploring single-cell analysis. Currently, her research focuses on advancing analytical methodology by combining SC- and LA-ICP-TOF-MS, with primary applications in biomedicine. Her work aims to understand the role of essential elements in cancer progression and to study NP-delivery of drugs, among other key bio-applications. In parallel, she applies her expertise in elemental 2D-mapping to interdisciplinary projects, including studies on biogenic carbonate materials in the context of sclerochronology and climate research. Despite being at an early stage of her career, Dr Lores Padín has established a strong international presence. She has presented her work at numerous national and international conferences, co-organized EWLA 2024 (Ghent, Belgium), and co-chaired sessions at SciX (US). Her contributions have been recognized with distinctions such as the 2022 SAS Atomic Student Award. She has also authored more than ten scientific publications in leading Q1 journals, as well as reviews and book chapters.

a powerful tool for resolving intricate microstructures and thus, for chronologically tracking bioaccumulation of environmentally relevant metals, offering significant advantages over traditional 1D (line scanning) analysis as the latter may lead to misinterpretation of elemental distributions.

Introduction

Biogenic carbonates, such as bivalve shells and otoliths, serve as natural chronological archives of past environmental conditions. Their incremental growth allows for the incorporation of major, minor, and trace elements from the surrounding environment into their calcium carbonate ($CaCO_3$) matrix, preserving chemical signatures that can remain unaltered over long (geological) timescales.[1] This makes them valuable archives as several proxies measured in carbonates can be relied on for reconstructing seasonal and long-term climate and environmental changes, biological processes, and even anthropogenic influences such as pollution episodes.[2] Utilizing the full potential of these records requires the use of a highly sensitive analytical technique with high spatial resolution (*i.e.*, $\leq$20 μm) capable of distinguishing micro-scale elemental and isotopic variations.[3]

Laser ablation – inductively coupled plasma-mass spectrometry (LA-ICP-MS) has been commonly used in the study of biogenic carbonates[4] due to its excellent limits of detection (LoDs, typically in the ng g^{-1} range), a linear dynamic range of up to 10 orders of magnitude, minimal sample preparation requirements and high sample throughput.[5] The technique has been used for both bulk (using large beam diameters, typically $\geq$100 μm) and microanalysis (bulk spot analysis and 1D-line scan analysis using spots typically ranging from 20 to 80 μm diameter).[6] Recent advances in LA technology, including the introduction of low-dispersion ablation cells[7,8] and transfer devices with improved aerosol transport efficiency,[9] have significantly enhanced the technique's capabilities. These developments now enable mapping with a spatial resolution down to approximately 1 μm and yield shorter single pulse response (SPR) profiles of $\leq$1 ms duration (defined as the width of the transient signal observed upon firing a single laser pulse at 10% of its maximum height). Furthermore, the integration of time-of-flight analyzers in ICP-MS instrumentation (ICP-TOF-MS), allowing quasi-simultaneous monitoring of nearly the entire periodic table (typically $^{23}Na^{+}$–$^{238}U^{16}O^{+}$) within just a few microseconds (<50 μs), has further expanded the applicability of LA-ICP-MS.[10] Together, these advances allow for rapid data acquisition at up to 1000 pixels per second, significantly boosting the technique's potential for ultra-fast, high-resolution, multi-elemental mapping.[11]

Despite significant advances in LA and ICP-MS instrumentation, accurate elemental quantification in carbonate matrices remains inherently challenging. This is primarily due to the matrix-dependent nature of the laser–sample interaction: with the commonly used nanosecond pulse lasers, the occurrence of thermal effects during the ablation process results in non-stoichiometric sampling and heterogeneous particle plumes, leading to elemental fractionation during ablation, aerosol transport and plasma processes such as particle vaporization and ion generation. In this context, apart from optimally tuning the LA parameters and ICP settings to minimize elemental fractionation ($^{238}U^{+}/^{232}Th^{+}$ signal ratio ~1 upon ablation of a NIST SRM 610 or 612 glass from the National Institute of Standards and Technology),[12,13] previous studies on carbonates have shown that also the laser wavelength exerts an important effect on the quantification. The use of a shorter laser wavelength, such as 193 nm, instead of 213 or 266 nm, enables more effective ablation of carbonate matrices due to the higher absorption efficiency, the formation of smaller particles (which significantly reduces vaporization-induced elemental fractionation), and reduced thermal effects.[14,15] This results in better defined craters and minimal sample fracturing upon ablation.[13,15,16] In addition, to further enhance analytical accuracy and precision in LA-ICP-MS applications, external calibration using certified reference materials (CRMs) or well-characterized in-house standards, combined with signal normalization based on the monitoring of an internal standard (IS), remains the most effective strategy.[5,17] However, the limited availability of homogeneous and compositionally representative carbonate-based reference materials continues to constrain robust quantification for such matrices.[13,18]

In response to these limitations, various calibration strategies have been evaluated, including both matrix-matched[13,19] and non-matrix-matched approaches[20] (using Ca as an internal standard in all cases). Traditionally, silicate glass reference materials, such as NIST SRM 610 and 612 have been employed owing to their excellent level of homogeneity and well-characterized composition.[21] However, Jochum *et al.*[13] demonstrated that non-matrix-matched calibration introduces a systematic bias of 10–20% in trace elemental concentrations due to differences in ablation efficiency and ion production in the plasma between silicate and carbonate matrices. While this approach remains suitable for refractory elements (*e.g.*, Ba, Sr), it is significantly less reliable for chalcophile and siderophile elements with a low boiling point (*e.g.*, Pb, Cu, Zn and Cd), an observation which supports the conclusions of a previous study by Kroslakova *et al.*[22] Consequently, matrix-matched calibration using $CaCO_3$-based RMs has become the preferred strategy.

Due to the lack of commercially available $CaCO_3$-based RMs, in-house calibration standards under the form of pressed powder pellets[23] or fused glass discs,[24] or obtained using co-precipitation methods[25–27] were developed. Although well-characterized, limitations in terms of contamination and poor elemental micro-homogeneity constrained their wide applicability. These limitations highlighted the need for well-characterized carbonate RMs, leading to the development of certified RMs such as USGS MACS-1 and MACS-3.[13,28] However, their coarse grain size (~10–15 μm) causes inefficient and unstable ablation behaviour, often resulting in elevated analytical uncertainties, cross-contamination, and memory effects during LA analysis.[16] In fact, Lazartigues *et al.*[29] reported

that using MACS-3 for obtaining quantitative high-resolution maps (*i.e.*, 5 μm pixel size) of small otoliths led to high relative standard deviations (RSDs) of 30–80% due to trace element heterogeneity as previously discussed.

A significant advancement in the field was the development of a novel carbonate pellet fabrication method by Garbe-Schönberg and Müller,[30] which enabled a reduction of the grain size to the sub-micron scale by implementing a 2-step milling procedure that uses a planetary ball mill for further grinding the material into a nanoscale powder after a freeze-drying step. The nanoparticulate powder, previously homogenized using a mixer mill to ensure uniform particle distribution, is pressed into pellets using a hydraulic press without the need of any binder. Jochum *et al.* demonstrated the potential of three novel "nanopellets": JCp-1-NP, JCt-1-NP (natural matrix source), and MACS-3NP (synthetic matrix source) showing a 2- to 3-fold higher uniformity in trace element distribution, leading to lower variability and higher accuracy in LA-ICP-MS spot analysis quantification.[30] JCt-1-NP and SPLT-NP (speleothem, natural matrix) have been recently used as external standard for 1D-elemental analysis (line profiling) of speleothems with 50 μm laser beam spots[19] as well as to enable accurate quantitative high spatial-resolution 2D-mapping of marine carbonates, using a laser spot size of ~2 μm.[31]

Typically, LA-ICP-MS analysis of carbonate archives relies on 1D analysis (line scanning) across a specimen's cross-section.[6,32] Such approach assumes homogeneous deposition of $CaCO_3$ and the other elements within well-defined growth layers. However, recent research has shown that elemental distributions within biogenic carbonates are often more heterogeneous than previously assumed, influenced by both environmental and biological factors that introduce structural discontinuities and variations in crystallization.[33] Such complexities can lead to misinterpretations, especially in areas lacking a clear chronological structure. In this context, two-dimensional (2D) elemental mapping offers a more comprehensive analytical approach, capturing the full spatial distribution of elements across the specimen. Although different 2D-mapping applications in carbonates using techniques like synchrotron X-ray fluorescence microscopy (SXFM) and wavelength-dispersive X-ray electron probe microanalysis (EPMA) have been employed for otolith analysis, they require long measurement times (often exceeding 8 hours for areas >4 mm^2) and access to large-scale synchrotron facilities.[34] EPMA provides high spatial resolution (<3 μm) but suffers from relatively poor detection limits (>10 μg g^{-1}).[33] Synchrotron- and lab-based micro-X-ray fluorescence analysis techniques have also aided in the 2D-characterization and speciation analysis of mollusc shell compositions.[35–38] While the resolution of these techniques (typically 20–50 μm spot size) approaches that of LA-ICP-MS, quantification limits (especially of lab-based systems) tend to be higher (~1 μg g^{-1}). Additionally, the long attenuation length of X-rays (>100 μm for energies needed to excite and measure Sr) has a tendency to integrate results below the sample surface, which can lead to time-averaging in incremental carbonate archives which often contain curved growth increments in three-dimensional space (see, *e.g.*, discussion in de Winter and Claeys, 2017).[35]

More recently, LA-ICP-TOF-MS has been applied to the study of biogenic structures, enabling fast multi-elemental 2D-mapping at high spatial resolution. For instance, otolith specimens were mapped using laser spot size of 4 μm at an acquisition rate of up to 25 pixels per s.[28] Coral samples have also been analysed using similar setups, employing even smaller spot sizes (1–2 μm) and faster acquisition rates (up to 200 pixels per s).[31] These advances demonstrate the capabilities of LA coupled to ICP-TOF-MS instrumentation, providing near-complete elemental coverage with high spatial resolution and high sample throughput in biogenic $CaCO_3$ applications.

Building on recent developments, this work presents the development of a quantitative method that enables fine-scale multi-elemental 2D-mapping of microstructural features in biogenic carbonate samples. This study has evaluated a new set of commercially available nanoparticulate pressed pellets, produced adapting the protocol described by Garbe-Schönberg and Müller,[30] for their micro-homogeneity and suitability as matrix-matched external calibration standards in high-resolution multi-elemental 2D-mapping. Unlike previous assessments using larger laser spot sizes (50–80 μm), we have tested their performance using significantly smaller beam diameters (5–20 μm) using a LA-unit equipped with a low-dispersion cell coupled to an ICP-TOF-MS system. The suitability of the nanopellets was evaluated for their use as external, matrix-matched standards for quantitative mapping of two types of biogenic carbonates commonly studied in sclerochronology: otoliths and mollusc shells. We use Ca internal normalization to correct for variations in ablation yield, potential matrix effects, and instrumental drift.

Experimental

Instrumentation

All experiments were carried out using an Iridia LA-unit equipped with a nanosecond 193 nm ArF* excimer-based laser system capable of firing laser pulses at a repetition rate up to 1 kHz. The laser unit comprises a Cobalt ablation chamber, equipped with a low-dispersion tube-type ablation cell (Teledyne Photon Machines). The tube cell was set at 500 μm distance to the sample surface for analysis. The Iridia was coupled to an icpTOF 2R ICP-TOF-MS unit (TOFWERK) using the Aerosol Rapid Introduction System (ARIS), consisting of PEEK tubing of 0.5 m length and 0.75 mm internal diameter and a co-axial mixing bulb for addition of the Ar make-up gas flow to the He carrier gas flow. The icpTOF 2R unit provides fast quasi-simultaneous monitoring and is capable of acquiring almost the entire elemental mass spectrum (from $^{23}Na^+$ to $^{238}U^{16}O^+$) every 46 μs. A specific dry plasma Ni sampling cone from TOFWERK AG was used to improve overall sensitivity and the collision/reaction cell was pressurized with pure H_2 (2 mL min^{-1}, ≥99.999% purity) which significantly suppresses the occurrence of argon-based species (*e.g.*, Ar^+, Ar_2^+, ArO^+) and boosts sensitivity, especially in the mid-to high-mass range due to collisional ion focusing.[39] NIST SRM 610 glass (Trace Elements in Glass, National Institute of Standards and Technology) was used for daily tuning of the LA-ICP-MS settings,

Table 1 Instrument settings and data acquisition conditions used in this work: icpTOF 2R and Iridia 193 nm LA-unit

LA unit		ICP-TOF-MS	
Carrier gas flow, He (L min^{-1})	1.05	RF power (W)	1550
Laser beam size (μm)	20 × 20 (2D LA-mapping), 10 × 10, 5 × 5	Sampling depth (mm)	5.2
Fluence (J cm^{-2})	4.0	Neb. Flow, Ar (mL min^{-1})	0.92
Repetition rate (Hz)	50 (2D LA-mapping), 2 (SPR & ODG opt)	CCT-mode, H_2 (mL min^{-1})	2.0
Dosage	1 (2D LA-mapping)	Notched masses (m/z)	40
Scan speed (mm s^{-1})	1.0	Notch amplitude (V)	1.0

aiming at high sensitivity across the elemental mass range ($^{59}Co^+$, $^{115}In^+$ and $^{238}U^+$), low oxide ion formation ($^{232}Th^{16}O^+/^{232}Th^+$ < 2%) and minimizing elemental fractionation ($^{238}U^+/^{232}Th^+ \sim 1$). The optimized instrument settings and data acquisition conditions used in this work are summarized in the Table 1. Note that for assessing of the single pulse response (SPR) profiles and setting the offset delay generator (ODG) time, sometimes referred to as aerosol transfer delay time, short integration times of <500 μs were required to define the signal peak in sufficient detail. The ODG is the total time it takes between firing an individual laser pulse and the arrival of ions at the Multi-Channel Plate (MCP). This value is required for adequate timing of the trigger signal of the laser system towards the ICP-TOF-MS unit. This offset delay is influenced not only by the matrix of the sample but also by instrumental parameters such as gas flow rates and torch position.

Standards and samples

In this study, several nanoparticulate (NP) powder-pressed pellets, manufactured by myStandards GmbH (Kiel, Germany), were examined. These pellets are manufactured according to a protocol first described by Garbe-Schönberg and Müller in 2014.[30] The resulting carbonate nanopowder is pressed into pellets with a diameter of 10 mm using a programmable hydraulic press. Notably, these pellets are pressed without binders to avoid potential contamination and matrix effects during laser ablation. For this work, the following nano-pellets were evaluated as matrix-matched external calibration standards: SPLT-NP-B01 (speleothem powder), NFHS-2-NP (foraminifera powder), ECRM-752-1*-NP (limestone powder), CRMS-NP-B01 (coral powder), BAM-RS3-NP ("RS3" powder, synthetic calcite), Apatite-NP-B01 (crystal apatite powder, note that this is a calcium phosphate matrix while the other nano-pellets have a calcium carbonate matrix), and BPLM-NP-B01 (Bivalve shell powder). The elemental compositions of Apatite-NP, BPLM-NP, and SPLT-NP have been certified in accordance with ISO 17035 and ISO Guide 35 (replaced by ISO 33405:2024). NFHS-2-NP was characterized as part of an international interlaboratory study.[40] In these cases, characterization was performed using ICP-MS, ICP-OES and WD-XRF following lithium-borate fusion and/or acid digestion. BAM-RS3-NP and ECRM-752-1*-NP were characterized for their elemental composition *via* solution-based ICP-MS after acid digestion of the nanopowder. All the nano-pellets contain 38–40 wt% Ca as the primary matrix component. The certificates of analysis can be found on the webpage of *myStandards*[41] and for some of the nano-pellets, the elemental composition can be found in the GeoRem database[42] as well. Data for specific target elements are displayed in the Results section for comparison and validation purposes (Tables 3 and S2)

Additionally, two types of biogenic carbonate samples were selected given their relevance in the context of microanalysis and the need for mapping at high spatial resolution. These samples serve as case studies to test the performance of the LA-ICP-TOF-MS setup on accretionary carbonate archives: (1) otoliths from two 6 year-old Atlantic cod fish (*Gadus morhua*), harvested from two locations in Norway—Store Lungegårdsvannet (Bergen) and Hardangerfjord. These specimens were provided by the Institute of Marine Research (IMR, Bergen, Norway). (2) Two different species of modern bivalve shells, the Pacific oyster (*Crassostrea gigas*) and the ocean quahog (*Arctica islandica*), were both harvested alive in the North Sea as part of previous studies[43,44] and provided by the Vrije University of Amsterdam (VUA, The Netherlands).

For all specimens, the samples were first cleaned and disinfected and then embedded in epoxy resin. They were sectioned dorsoventrally along their axis of maximum growth in thin sections (tens of microns), these sections were polished and mounted onto microscope slides (Corning®, Merck 75 mm × 25 mm) with double-sided tape or adhesive to ensure proper fixation and prevent alteration during subsequent LA-ICP-TOF-MS analysis.

Data processing

Chromium v3.2.8 and TOFWERK TOFPilot v2.15.9.0 software were used to operate the Iridia LA-unit and icpTOF 2R ICP-TOF-mass spectrometer and record the elemental mass spectra, which were stored in HDF5 files, an open-source hierarchal data format, along with all experimental metadata. The data analysis package TOFware Igor Pro v3.2.3 was used for processing the elemental mass spectra obtained, including performing the time-dependent mass calibration, modelling and subtracting of the baseline signal intensities, and peak shape determination and integration. HDIP software version 1.8.184 from Teledyne Photon Machines was used to spatially reconstruct the multi-elemental 2D-maps. It was also used for constructing the calibration curves based on external calibration using the reference materials and IS normalization. The peak detection tool enabled reconstructing the average SPR profiles and calculating integrated signal intensities as well as SPR durations. Additionally, Microsoft Excel software was employed for the data treatment of the nano-pellets study and for constructing graphs.

Results & discussion

LA-ICP-TOF-MS method optimization for the $CaCO_3$ matrix

For successful analysis of $CaCO_3$ sample matrices using LA-ICP-TOF-MS, it is essential to achieve sufficient sensitivity for the reliable detection of major, minor, and trace elements across the entire elemental mass range, while paying attention to the linear dynamic range avoiding detector saturation due to the high signal intensities originating from major elements (*e.g.*, Ca). Thus, the use of Collision/Reaction Cell Technology (CCT) with hydrogen (H_2) gas was evaluated to suppress Ar-based polyatomic interferences and boost the sensitivity as a result of collisional focusing. The sensitivity was monitored at different H_2 gas flow rates (0–6 mL min^{-1}) while ablating a NIST SRM 610 glass and in Fig. 1A, the sensitivities obtained for the target nuclides ^{24}Mg, ^{52}Cr, ^{56}Fe, ^{88}Sr, ^{137}Ba, ^{232}Th and ^{238}U are displayed. It was found that pressurizing the cell with pure H_2 at a flow rate of 2 mL min^{-1} increased sensitivity by approximately 1.7-fold for the high-mass range, *e.g.*, ^{232}Th, and ^{238}U, and 1.5-fold for the mid-mass range, *e.g.*, ^{52}Cr, ^{56}Fe, and ^{88}Sr and ^{137}Ba, while slightly reducing the sensitivity for lighter elements such as ^{24}Mg which is in accordance with observations previously reported by Burger *et al.*,[45] when using a mix of H_2/He. Moreover, the use of H_2 also attenuated the signal intensity of polyatomic ions, such as ArO^+ interfering with the monitoring of $^{56}Fe^+$ and other Ar-containing ions,[39] including $^{40}Ar^+$. In general, by using a low flow rate (*i.e.*, ~2 mL min^{-1} of H_2) the signal-to-noise ratio (SNR) was improved by decreasing the background levels (Fig. S1A). Therefore, finding a balance between reaching high sensitivity for detecting minor and trace elements and avoiding overloading the ICP-TOF-MS detector with intense signals from major elements like Ca (which represents ~40% of the total mass) is crucal for both nano-pellets and samples. To mitigate the latter risk, the most abundant isotope, $^{40}Ca^+$, was attenuated using the notch filter to prevent detector saturation (see Table 1 for notching filter details), though even less abundant isotopes such as $^{43}Ca^+$ and $^{44}Ca^+$ still produced highly intense signals as shown in the mass spectrum below observed upon ablation of NFHS-2-NP (Fig. 1B). Additionally in Fig. 1C, a part of the mass spectrum is displayed, zoomed in on the low mass range between 36–47 amu. Removing $^{40}Ca^+$ using the notch filter also affected the signal of neighbouring masses such as that for $^{42}Ca^+$, as a result of which its signal intensity was lower than that of $^{43}Ca^+$, despite the higher natural relative abundance (0.647% *vs.* 0.135% for ^{42}Ca and ^{43}Ca, respectively). It is also important to consider hydride formation when H_2 is used as a reaction gas, for instance, while the $^{36}Ar^+$ peak is almost negligible, a significant $^{36}ArH^+$ signal can be observed at m/z 37. Although ThO^+/Th^+ ratios increased from <1% (0 mL min^{-1}, standard mode) to 2.8% (6 mL min^{-1}), they remained below 1.5% at 2 mL min^{-1} H_2, with no observable effect on mass fractionation as the H_2 flow rate was increased in the CCT showing a U^+/Th^+ ratio ~1 at all H_2 flows tested (Fig. S1B).

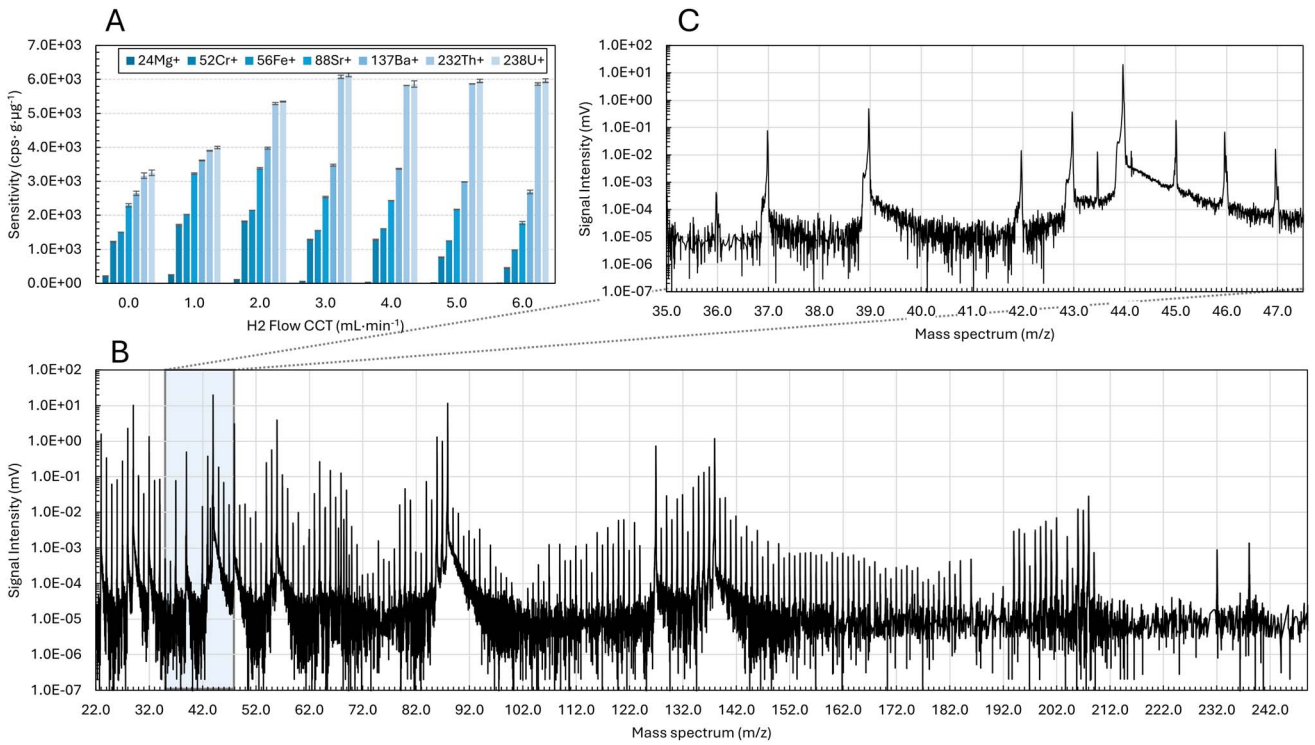

Fig. 1 icpTOF 2R optimization in CCT mode by pressurizing the cell with H_2: (A) ICP-TOF-MS sensitivity (cps per µg g^{-1}) for selected nuclides (^{24}Mg, ^{52}Cr, ^{56}Fe, ^{88}Sr, ^{137}Ba, ^{232}Th and ^{238}U) at different H_2 flow rates (0, 1, 2, 3, 4, 5, and 6 mL min^{-1}), (B) average raw full mass spectrum exported from TofDaq obtained upon ablation of NFHS-2-NP using a 20 × 20 $µm^2$ square spot size, 4 J cm^{-2} of laser fluence and 2 mL min^{-1} of H_2 introduced into the CRC. (C) Mass spectrum zoomed in on the m/z range from 36–47 amu). The notch filter was applied to attenuate the intense $^{40}Ca^+$ signal, which also partially suppressed the signal at the neighbouring masses.

At the LA-side, it was evaluated whether for a laser beam size of 20 × 20 μm^2 (square mask) different laser fluences of 2, 3, 4 and 5 J cm^{-2} were capable of effectively ablating the $CaCO_3$ matrix. Using the NFHS-2-NP nano-pellet as a $CaCO_3$ matrix reference, increasing the fluence from 2 to 4 J cm^{-2} resulted in improved sensitivity across all examined elements (by a factor of 1.5), including those present at low (<1 μg g^{-1}; *e.g.*, Co, Cr, Pr, U, Th), mid (1–20 μg g^{-1}; *e.g.*, Ce, Pb, Cu, Zn), and high concentrations (>20 μg g^{-1}; *e.g.*, Na, Mn, Mg, Al, Fe, Sr), as shown in Fig. 2. However, increasing the fluence beyond 4 J cm^{-2} to 5 J cm^{-2} resulted in a slight enhancement of <5% only, thus 4 J cm^{-2} was selected as the optimal value ensuring effective carbonate ablation.

Evaluation of the micro-homogeneity of nano-pellets using LA-ICP-TOF-MS

To evaluate the elemental micro-homogeneity of the different nano-pellets, firstly, a qualitative study was carried out by performing 2D-mapping for each individual nano-pellet from the set. Therefore, the duration of the SPR profiles and the ODG had to be assessed for this specific matrix type. Thus, by using the parameters described above (*i.e.*, 20 × 20 μm^2 beam size and 4 J cm^{-2} fluence and the gas flows summarised in Table 1), the SPR duration defined as FW0.1 M was found to be approximately 20 ms, which restricted the pixel acquisition rate to 50 pixels/s. The laser repetition rate was set to 50 Hz and only a single shot was fired per pixel position (dosage of 1). Note that apart from the matrix type and the parameters described above, also the PEEK transport tubing length, positioning of the ARIS with respect to the torch injector, as well as the He flow rates play a role in achieving well-shaped and constant SPRs.

Simultaneous 2D multi-element mapping of 3 × 1 mm^2 regions of interest (ROIs) were performed for each nano-pellet (corresponding to 3.82% of the total nano-pellet surface) using LA-ICP-TOF-MS, generating a total of 7500 data points (*i.e.*, pixels in the 2D-map), corresponding to 50 lines of 3 mm length per pellet (1 line = 150 data points). Visual inspection of the qualitative ^{44}Ca normalized maps for selected target elements present in the nano-pellets reveals the degree of homogeneity. For instance, Fig. 3 allows visual comparison between NFHS-2-NP and BPLM-NP nano-pellets. While NFHS-2-NP shows a high degree of micro-homogeneity for all the target elements, even those prone to surface contamination such as Zn, in BPLM-NP elements such as Al, Mn, Fe, Cu, Zn and Pb show a less homogeneous distribution. This is also the case for other nano-pellets (Fig. S2), with BAM-RS3-NP exhibiting more heterogeneity compared to the more uniform distribution observed in CRMS-NP or ECRM-752-1-NP.

In addition, also the repeatability based on the relative standard deviation (RSD) of the average signal intensity for independent line scan measurements was evaluated (total lines, n = 50 & sub-sets n = 25, 10, 5 and 3) and compared to values obtained for NIST SRM 610 glass (RSDs <2%, Table S1). For example, while NFHS-2-NP exhibited RSD values between 1% and 7% across all elements (Table 2, top), for BPLM-NP, RSDs for elements such as Cu, Zn and Pb RSDs were as high as ~60%, ~80% and ~47%, respectively (Table 2, bottom). When randomly selecting subsets of 25, 10, 5 and 3 lines (3750, 1500, 750 and 450 data points, respectively) from the full set of 50 (7500 data points), in all cases, the calculated RSDs as well as the average signal intensity remained similar to those calculated from the full dataset (see Table 2 for NFHS-2-NP and BPL M-NP, and Table S1 for an overview covering all target elements and the entire set of nano-pellets). Notably, due to the heterogeneous distribution of certain elements, the RSD could fluctuate significantly depending on the lines selected. For example, Pb in BPLM-NP showed an RSD of nearly 50% when calculated based on 10 lines, but this dropped to a value of 7% when only 3 lines were used. Similar observations were made for BAM-RS3-NP (see Table S1). This behaviour indicates high spatial heterogeneity in certain elemental distributions, as seen in the corresponding maps (Fig. 3 and S2). However,

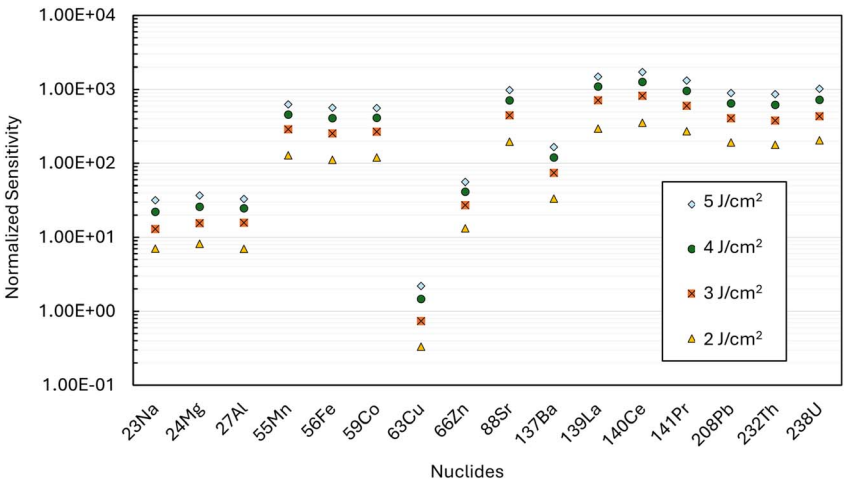

Fig. 2 ^{44}Ca$^+$-normalized sensitivities for selected nuclides in the low-, mid-, and high-mass range, measured for an NFHS-2-NP pressed powder pellet upon ablation at laser fluences of 2, 3, 4, and 5 J cm^{-2}. A laser beam size of 20 × 20 μm^2 was used. The relative standard deviation (RSD) was <5% for all nuclides shown (n = 3 independent ablation lines).

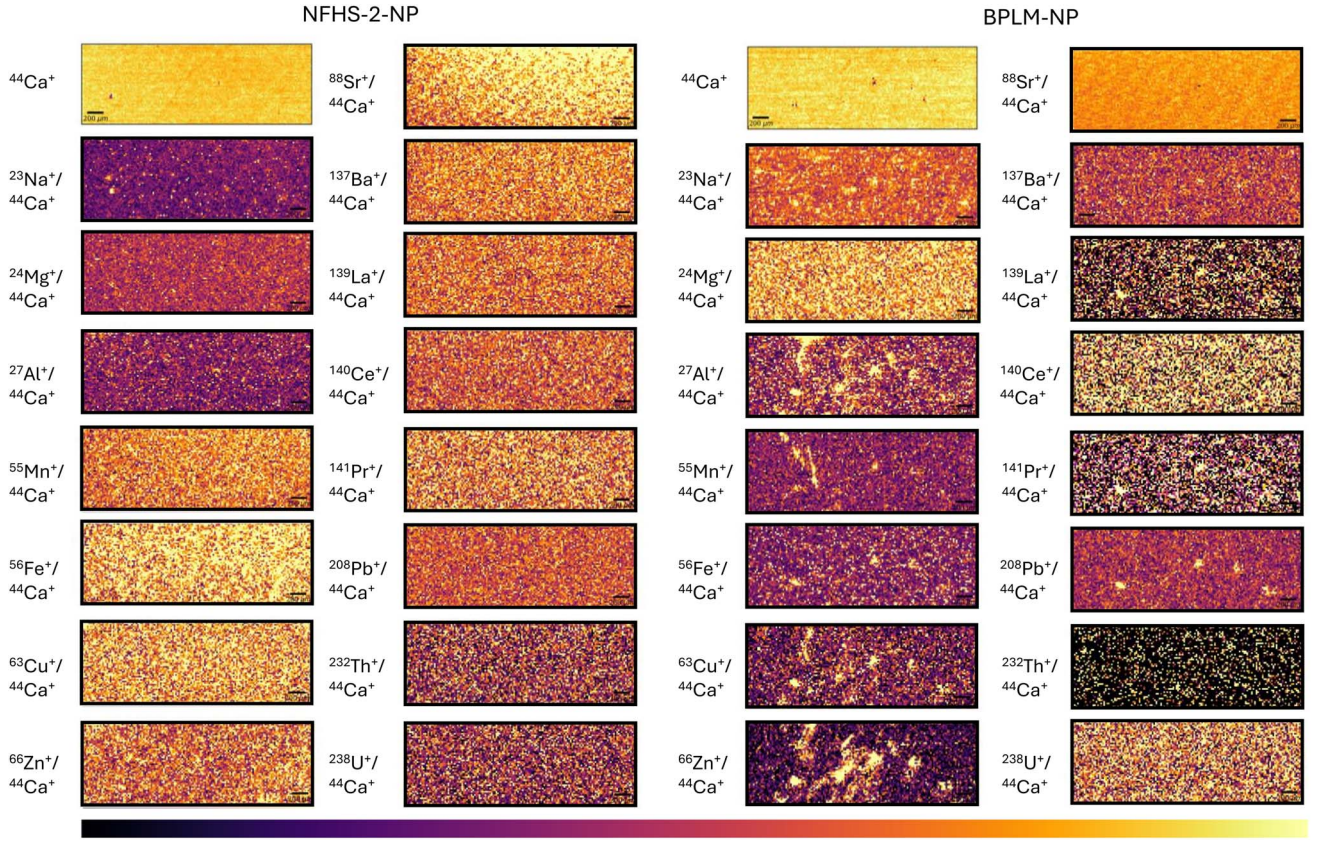

Fig. 3 Qualitative 2D elemental maps normalized to ^{44}Ca (3 mm × 1 mm, with 20 × 20 μm^2 laser beam) for ^{24}Mg, ^{27}Al, ^{55}Mn, ^{56}Fe, ^{63}Cu, ^{66}Zn, ^{88}Sr, ^{137}Ba, ^{139}La, ^{140}Ce, ^{141}Pr, ^{208}Pb, ^{232}Th and ^{238}U in NFHS-2-NP and BPLM-NP pressed powder pellets. The scale bar indicates 200 μm and the colour bar indicates the intensity based on the nuclide/$^{44}Ca^+$ ratio from min to max (always from 0 to each max value).

while the average signal intensities may vary depending on the number of lines (n) selected—up to 20% for Zn in BPLM—most elements showed a variation < 5% across all nano-pellets (Table S1), supporting the high micro-homogeneity of the nano-pellets.

Higher uncertainties tend to correlate with lower elemental concentrations, especially for elements present at or below the μg g^{-1} level. In Fig. 4, plotting the RSD% (based on 10-line measurements) against the element mass fraction (μg g^{-1}) across all nano-pellets reveals a general trend: elements at higher concentrations exhibit lower RSDs. However, this trend is not consistent across all materials. In the case of NFHS-2-NP, RSDs remained below 5% for elements above 1 μg g^{-1} with an increase to 20% for concentrations below the μg g^{-1} level. However, in other nano-pellets, like CRMS-NP or Apatite-NP, elements around 5–100 μg g^{-1} displayed higher RSDs than some sub-μg g^{-1} elements, suggesting that concentration alone does not fully explain the variability. Overall, except for elements at sub-μg g^{-1} levels in BPLM-NP and BAM-RS3-NP (RSDs in the range of 50–100%), RSD values remained within acceptable limits—mostly below 30%, and in some pellets (*e.g.*, NFHS-2-NP) under 10%. This result matches the RSDs found by Jochum *et al.*[18] when evaluating the first ever nanoparticulate pellets (MACS-3NP, JCp-1NP and JCt-1-NP) using larger spot sizes (25 and 55 μm), who reported RSDs between 2–30% ($n = 9$ lines of 200 μm length.

Additionally, calibration curves were constructed based on the average signal intensities normalized to $^{44}Ca^+$ obtained upon ablation of 50- and 3-line scans for all 7 nano-pellets and the slope and linearity were compared accordingly (Fig. 5). As an example, the calibration curves for four target elements—Mn, Zn, Sr, and Ba—are shown. Overall, for most elements, no significant differences in linearity (coefficient of determination, r^2) or sensitivity (slope) were observed between the two approaches. However, for Zn, a deviation was detected: the slope of the calibration curve increased from 14.12 to 15.7 when using $n = 3$ lines instead of $n = 50$, representing an ~11.2% increase. This variation can be attributed to the lower Zn concentrations in certain nano-pellets and the higher micro-scale heterogeneity observed. Despite this, a change of approximately 11% in the slope remains within acceptable limits for many applications, depending on the required level of accuracy and the overall uncertainty tolerance of the method.

Elemental characterization of the nano-pellets using smaller laser beam sizes

Certified elemental concentrations in nano-pellets are normally determined through bulk analysis, either using solution ICP-MS

Table 2 Calculated RSDs based on the average signal intensities of individual lines from the elemental 2D-maps for nano-pellets: NFHS-2-NP (top) and BPLM-NP (bottom). The average signal intensities and the corresponding RSDs are shown for sets of 50, 25, 10, 5, and 3 lines. Information for the entire range of target elements as well as for the rest of the nano-pellets is available in the SI (Table S1)

NFHS-2-NP	^{55}Mn		^{56}Fe		^{63}Cu		^{66}Zn		^{88}Sr		^{137}Ba		^{208}Pb		^{238}U	
n	Mean (cts)	RSD	Mean (cts)	RSD	Mean (cts)	RSD	Mean (cts)	RSD	Mean (cts)	RSD	Mean (cts)	RSD	Mean (cts)	RSD	Mean (cts)	RSD
50	2.14×10^2	1%	6.83×10^1	2%	6.58×10^0	4%	6.68×10^0	7%	6.26×10^3	1%	1.11×10^2	2%	2.15×10^1	2%	2.35×10^0	8%
25	2.13×10^2	1%	6.82×10^1	2%	6.66×10^0	4%	6.55×10^0	4%	6.26×10^3	1%	1.12×10^2	2%	2.14×10^1	2%	2.35×10^0	9%
10	2.14×10^2	1%	6.86×10^1	2%	6.72×10^0	5%	6.55×10^0	5%	6.28×10^3	1%	1.12×10^2	2%	2.14×10^1	2%	2.41×10^0	13%
5	2.15×10^2	1%	6.90×10^1	1%	6.64×10^0	7%	6.64×10^0	7%	6.28×10^3	1%	1.13×10^2	3%	2.12×10^1	3%	2.36×10^0	7%
3	2.15×10^2	1%	6.83×10^1	2%	6.75×10^0	6%	6.78×10^0	5%	6.28×10^3	1%	1.13×10^2	3%	2.15×10^1	3%	2.37×10^0	8%
BPLM-NP	^{55}Mn		^{56}Fe		^{63}Cu		^{66}Zn		^{88}Sr		^{137}Ba		^{208}Pb		^{238}U	
n	Mean (cts)	RSD	Mean (cts)	RSD	Mean (cts)	RSD	Mean (cts)	RSD	Mean (cts)	RSD	Mean (cts)	RSD	Mean (cts)	RSD	Mean (cts)	RSD
50	7.94×10^0	12%	1.12×10^1	10%	2.65×10^0	48%	2.72×10^0	84%	8.75×10^3	1%	8.09×10^0	4%	9.00×10^0	27%	2.62×10^0	7%
25	7.95×10^0	14%	1.16×10^1	11%	3.12×10^0	51%	3.34×10^0	77%	8.77×10^3	1%	8.19×10^0	4%	9.57×10^0	33%	2.59×10^0	7%
10	8.19×10^0	21%	1.12×10^1	8%	3.35×10^0	61%	4.36×10^0	85%	8.76×10^3	1%	8.26×10^0	3%	1.03×10^1	47%	2.62×10^0	9%
5	7.46×10^0	6%	1.06×10^1	4%	2.28×10^0	8%	3.35×10^0	83%	8.80×10^3	2%	8.15×10^0	2%	8.27×10^0	2%	2.63×10^0	6%
3	8.42×10^0	31%	1.07×10^1	5%	2.25×10^0	8%	2.25×10^0	8%	8.70×10^3	1%	8.14×10^0	2%	8.58×10^0	7%	2.55×10^0	3%

after acid digestion of the nanoparticulate powder or, in some cases, using LA-ICP-MS analysis of the nano-pellet using a relatively large laser beam diameter (50–80 μm). In this section, the effect of using significantly smaller laser beam sizes (*i.e.*, square shape of 20 × 20, 10 × 10 and 5 × 5 μm^2) on the quantitative results of LA-ICP-MS elemental analysis is addressed. Two different quantification approaches were applied: (1) non-matrix-matched method using NIST SRM 610 glass as an external calibration standard with Ca as IS to correct for differences in ablation yield between the silicate glass and carbonate matrices. This method mirrors the approach traditionally used for elemental analysis of the nano-pellets. (2) Matrix-matched external calibration, in which each nano-pellet was quantified using a calibration curve constructed based on the remaining full ($N - 1$) set of nano-pellets. The results from both approaches are compared with one another and with the reference values provided for the nano-pellets. In addition, the feasibility of using a single nano-pellet (1-point calibration) for analysis of the other nano-pellets was tested.

Table 3 presents the results obtained for CRMS-NP (top) and NFHS-2-NP (bottom) using a 20 × 20 μm^2 square laser beam. Decreasing the laser beam size reduces the ablation yield and thus, the relative sensitivity. As a result, signal intensities are lower, and the uncertainty becomes higher, both negatively affecting the accuracy when using a non-matrix-matched approach. In particular, low recoveries were observed for light elements such as Na, Al, and Zn, with biases ranging between 50% and 70% for both nano-pellets (Table 3, top and bottom). Significant deviations from the reference values were also found for low-concentration elements. For example, for Pr, Th, and U in CRMS-NP, and La, Ce, Pr, Pb, Th, and U in NFHS-2-NP, the results showed 40–50% bias when compared to the reference value. In contrast, with matrix-matched external calibration—particularly when applying Ca as an IS—the accuracy improved significantly (see column 4 and 5 in Table 3). Most data obtained using this method showed a bias <12%, with only a few exceptions (mainly sub-ppm elements, present at a concentration close to the corresponding LOQ) showing a bias up to 20%. These values remain within acceptable limits for trace element analysis, demonstrating the effectiveness of the matrix-matched strategy for reliable quantification.

It is important to emphasize the importance of using Ca as an IS in this type of application—not only when the matrix of the calibration material differs from that of the sample, but also when using nano-pellets composed of similar yet non-identical carbonate matrices for calibration. As shown in Table 3, recoveries were significantly improved when Ca was used as an IS in external calibration against nano-pellets. This is illustrated by the calibration curves (Fig. S3), for which omission of Ca as IS resulted in poor linearity. For example, R^2 values of 0.5274 (Al), 0.7803 (Sr), and 0.8642 (Mn) improved to 0.9969, 0.9965, and 0.9990, respectively, when Ca was applied as an IS. These results highlight the variability in ablation behaviour even among carbonate-based materials, particularly in the case of Apatite, which has a distinct $Ca_5(PO_4)_3(F, Cl, OH)$ crystal structure, which deviates significantly from that of typical carbonate matrices. Using an IS significantly improved

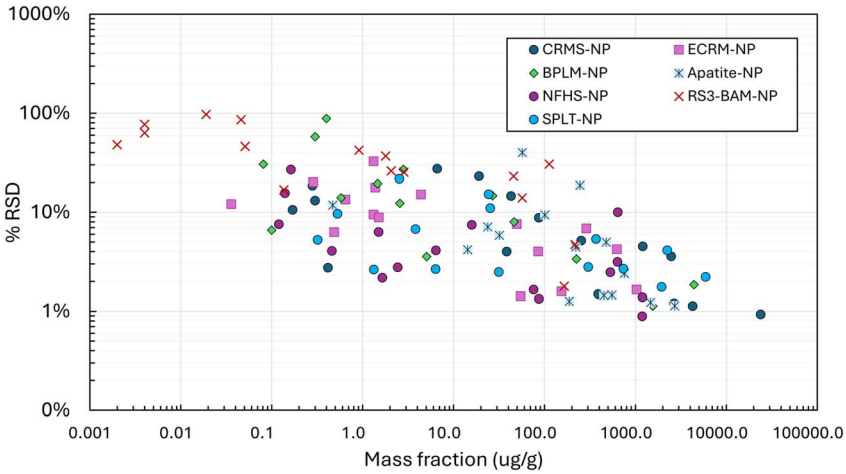

Fig. 4 RSD% based on 10 individual line scans performed for the entire set of nano-pellets (CRMS-NP, ECRM-752-1-NP, BPLM-NP, Apatite-NP, NFHS-2-NP, BAM-RS3-NP and SPLT-NP), plotted as a function of the mass fraction (μg g^{-1}) of the elements present.

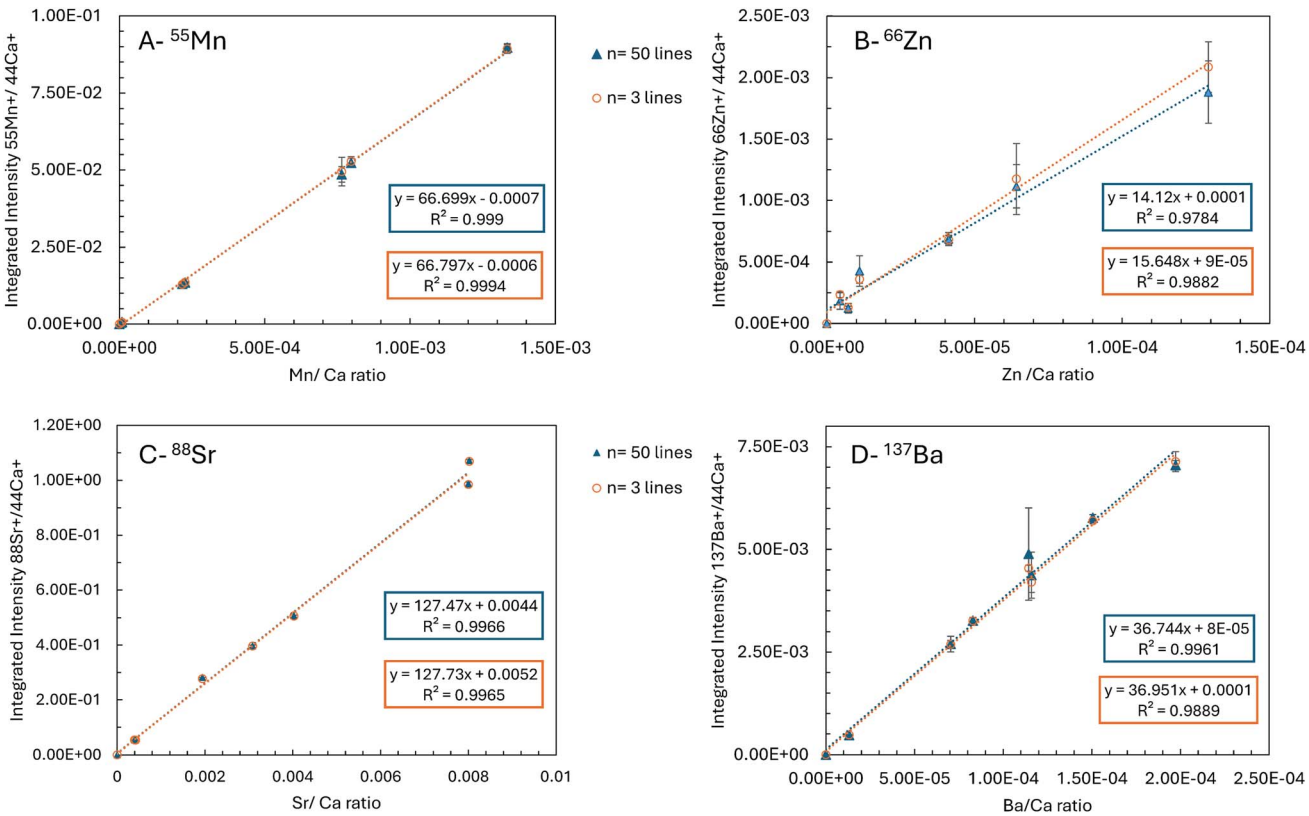

Fig. 5 Comparison of the linearity and slopes of calibration curves constructed based on the average signal intensities for 50 (triangles and blue boxes) and 3-line scans (circles and orange boxes) for (A) $^{55}Mn^+$, (B) $^{66}Zn^+$, (C) $^{88}Sr^+$, and (D) $^{137}Ba^+$, respectively, and normalized to $^{44}Ca^+$. Each point of the calibration curve represents the integrated intensity for a given nano-pellet, with the X/Ca ratios calculated based on the reference values. Error bars indicate the standard deviation (SD) of the average normalized signal intensities. In some cases, error bars are not visible due to the low SDs.

the linearity of all calibration curves, resulting in an average R^2 value of 0.9958 ± 0.0048 across all target elements. Also, small variations in laser beam focus during ablation could negatively affect the linearity which can be overcome when using internal standardization.

The recoveries obtained for the target elements in the remaining nano-pellets (Apatite-NP, SPLT-NP, BAM-RS3-NP, ECRM-752-1-NP and BPLM-NP) are shown in the SI (Table S2). The results highlight a clear relationship between the micro-homogeneity of nano-pellets and the accuracy of elemental

Table 3 Results for two of the nano-pellets investigated: CRMS-NP (upper pane) and NFHS-2-NP (lower pane). Summary of the calculated concentrations for the target elements by using different quantification approaches: (1) non-matrix-matched calibration against NIST SRM 610 with Ca as IS, (2) matrix-matched calibration using the full set of nano-pellets without IS, (3) matrix-matched calibration using the full set of nano-pellets with Ca as IS, and (4) matrix-matched calibration against a single nano-pellet standard (final column). NFHS-2-NP was used to quantify CRMS-NP, and *vice versa*. The propagated uncertainty is expressed as sd based on $n = 3$ lines used in the calibration, combined with the uncertainty from the certified concentration values (first column)

CRMS-NP	Reference value		Against NIST SRM 610/Ca (IS)				Against nano-pellets CAL				Against nano-pellets CAL/Ca (IS)				Against NFHS-2-NP/Ca (IS)					
Element	Conc. (μg g^{-1})	sd	Conc. (μg g^{-1})	sd	RSD %	Recovery %	Conc. (μg g^{-1})	sd	RSD %	Recovery %	Conc. (μg g^{-1})	sd	RSD %	Recovery %	Conc. (μg g^{-1})	sd	RSD %	Recovery %	LOD (μg g^{-1})	LOQ (μg g^{-1})
Na	4270	160	1398	16	1%	33%	55 780	63	1%	131%	4640	52	1%	109%	4920	230	5%	115%	55	180
Mg	23 940	690	21 570	200	1%	90%	25 050	230	1%	105%	23 980	220	1%	100%	26 540	920	3%	111%	1.7	5.8
Al	1207	38	441	20	5%	37%	2550	120	5%	211%	1140	52	5%	94%	1080	140	13%	89%	2.9	9.8
P	521	26	673	16	2%	129%	580	13	2%	111%	590	14	2%	112%	550	13	2%	106%	100	340
Mn	254	17	247	13	5%	97%	415	21	5%	163%	240	13	5%	96%	270	14	5%	108%	0.20	0.65
Fe	2479	88	2076	56	3%	84%	3368	91	3%	136%	2340	63	3%	94%	2150	160	8%	87%	0.22	0.72
Cu	86.8	5.7	92.6	8.2	9%	107%	88.4	7.8	9%	102%	87.0	7.7	9%	100%	109	11	10%	126%	0.19	0.63
Zn	42.9	3.2	34.7	7.5	21%	81%	50.7	13.6	27%	118%	44.2	5.9	13%	103%	41.0	6.7	16%	96%	0.15	0.52
Sr	2663	59	2618	31	1%	98%	3620	220	6%	136%	2770	120	4%	104%	2770	110	4%	104%	0.021	0.071
Cd	0.30	*	0.335	0.044	13%	112%	0.568	0.074	13%	189%	0.35	0.10	29%	115%	0.31	0.10	32%	102%	0.28	0.92
Ba	38.5	2.3	34.6	4.4	13%	90%	60.4	7.8	13%	157%	39.7	5.1	13%	103%	38.5	2.3	6%	100%	0.16	0.53
La	6.62	1.40	5.21	1.72	33%	79%	11.7	3.2	27%	176%	7.1	2.1	30%	107%	6.8	2.3	34%	103%	0.0070	0.023
Ce	19.1	5.0	15.7	3.6	23%	82%	29.0	6.7	23%	152%	17.6	2.0	12%	92%	20.3	1.9	9%	106%	0.0046	0.015
Pr	0.281	0.041	0.231	0.043	19%	82%	0.506	0.094	19%	180%	0.310	0.057	19%	110%	0.310	0.069	22%	110%	0.0054	0.018
Pb	391	*	332.5	4.9	1%	85%	391.2	6.2	2%	100%	391.0	6.2	2%	100%	397.2	2.6	1%	102%	0.032	0.11
Th	0.1700	0.03	0.112	0.012	11%	66%	0.327	0.035	11%	192%	0.200	0.021	11%	117%	0.1648	0.0012	1%	97%	0.010	0.034
U	0.4160	0.037	0.2861	0.00051	<1%	69%	0.6119	0.0011	<1%	147%	0.37190	0.00067	<1%	89%	0.523	0.012	2%	126%	0.0090	0.030

NFHS-2-NP	Certified value		Against NIST SRM 610/Ca (IS)				Against nano-pellets CAL				Against nano-pellets CAL/Ca (IS)				Against CRMS-NP					
Element	Conc. (μg g^{-1})	sd	Conc. (μg g^{-1})	sd	RSD %	Recovery %	Conc. (μg g^{-1})	sd	RSD %	Recovery %	Conc. (μg g^{-1})	sd	RSD %	Recovery %	Conc. (μg g^{-1})	sd	RSD %	Recovery %	LOD (μg g^{-1})	LOQ (μg g^{-1})
Na	1195	52	340	32	9%	28%	880	47	5%	74%	1140	36	3%	95%	1037	35	3%	87%	55	180
Mg	637	28	520	16	3%	82%	387.0	5.8	2%	61%	574.0	8.7	2%	90%	575	11	2%	90%	1.7	5.8
Al	641	45	260	26	10%	41%	940	20	2%	147%	660	14	2%	102%	718	24	3%	112%	2.9	9.8
P	91.0	8.0	<LOQ	*	*	*	<LOQ	*	*	*	<LOQ	*	*	*	<LOQ	*	*	*	100	340
Mn	87.00	0.35	79.8	1.1	1%	92%	87.0	1.2	1%	100%	80.0	1.1	1%	91%	80.8	1.8	2%	93%	0.20	0.65
Fe	532	36	513	11	2%	96%	530	15	3%	100%	580	16	3%	108%	612	25	4%	115%	0.22	0.72
Cu	6.40	0.30	6.10	0.25	4%	95%	3.80	0.25	6%	60%	5.80	0.38	6%	91%	5.09	0.13	3%	80%	0.19	0.63
Zn	15.9	1.5	15.0	1.1	8%	93%	13.80	0.72	5%	87%	18.62	0.98	5%	117%	16.63	0.87	5%	105%	0.15	0.52
Sr	1190	45	1120	10	1%	94%	1000	12	1%	84%	1186	14	1%	100%	1147	11	1%	96%	0.021	0.071
Cd	0.1630	0.0090	<LOD	*	*	*	<LOD	*	*	*	<LOD	*	*	*	<LOD	*	*	*	0.28	0.92
Ba	76.0	1.0	65.0	1.1	2%	85%	74.0	2.5	3%	97%	75.3	2.6	3%	99%	76.0	1.3	2%	100%	0.16	0.53
La	2.43	0.11	1.860	0.052	3%	77%	2.710	0.076	3%	111%	2.554	0.072	3%	105%	2.300	0.040	2%	95%	0.0070	0.023
Ce	1.50	0.10	1.160	0.073	6%	77%	1.390	0.087	6%	93%	1.310	0.082	6%	87%	1.410	0.090	6%	94%	0.0046	0.015

Table 3 (*Contd.*)

NFHS-2-NP	Certified value		Against NIST SRM 610/Ca (IS)				Against nano-pellets CAL				Against nano-pellets CAL/Ca (IS)				Against CRMS-NP					
Element	Conc. ($\mu g\ g^{-1}$)	sd	Conc. ($\mu g\ g^{-1}$)	sd	RSD %	Recovery %	Conc. ($\mu g\ g^{-1}$)	sd	RSD %	Recovery %	Conc. ($\mu g\ g^{-1}$)	sd	RSD %	Recovery %	Conc. ($\mu g\ g^{-1}$)	sd	RSD %	Recovery %	LOD ($\mu g\ g^{-1}$)	LOQ ($\mu g\ g^{-1}$)
Pr	0.460	0.040	0.340	0.014	4%	73%	0.480	0.014	3%	104%	0.452	0.013	3%	98%	0.410	0.050	12%	89%	0.0054	0.018
Pb	1.650	0.050	1.370	0.030	2%	83%	1.030	0.027	3%	63%	1.600	0.042	3%	97%	1.624	0.030	2%	98%	0.032	0.11
Th	0.140	0.010	0.100	0.015	16%	69%	0.170	0.013	8%	123%	0.163	0.012	8%	116%	0.144	0.020	14%	103%	0.010	0.034
U	0.120	0.030	0.0660	0.0050	8%	55%	0.0910	0.0074	8%	76%	0.0855	0.0070	8%	71%	0.10	0.012	13%	79%	0.0090	0.030

quantification. Nano-pellets with poorer homogeneity—evidenced by a more heterogenous elemental distribution as also evidenced by higher relative standard deviations (RSDs) on the signal intensities/element concentration values as discussed in the previous section—tend to yield less favourable recoveries for the elements affected. This is particularly evident in the case of BAM-RS3 and BPLM-NPs. For example, in BPLM-NP, the recovery for Th was <30%, likely due to its sub-ppm concentration close to the LOQ combined with the pellet's higher heterogeneity. For BAM-RS3-NP, poor accuracies were obtained for most of the elements (*e.g.*, Fe ~30%, Mn ~138% and Zn ~229%). A similar observation was made for the ECRM-752-1 nano-pellet: while the nano-pellet-based calibration improved overall accuracy, limitations remain for specific elements like Zn, (recovery of ~190%). In other cases, like for Apatite-NP, quantification using the non-matrix-matched approach (NIST SRM 610 glass) was accurate for certain elements, such as Sr, Ba, La or Ce, only, all showing less than 10% bias. However, for the majority of elements, recoveries were highly inaccurate (Table S2). In contrast, the matrix-matched approach using nano-pellets significantly improved performance, yielding recoveries between 86% and 119% across all target elements. Overall, elements present at sub-$\mu g\ g^{-1}$ concentration (especially those close to the LOQ), as well as elements prone to contamination such as Zn show poorer accuracies even when using a matrix-matched calibration and Ca normalization.

In a next phase, the comparison between the outcomes using the full set of nano-pellets for calibration and using a simplified one-point calibration approach, were compared. In this case, only NFHS-2-NP and CRMS-NP, selected based on their superior micro-homogeneity and covering the majority of target elements (above their LOD), were used as one-point calibration standards. For all target elements (except for Cu and U with uncertainties reaching 30%) the average offset from the reference value was below 20% for CRMS-NP, NFHS-NP and SPLT-NP, highlighting the potential of one-point calibration using well-characterized, homogeneous standards (Fig. 6A–C, respectively). However, a trend towards higher uncertainties was observed when using one-point calibration compared to the full calibration curve for the entire set of nano-pellets (Fig. 6). Particularly for Apatite-NP, offsets for most elements increased from 10% (dark green area) to nearly 30%, and for ECRM-752-1-NP, deviations from the reference values reached up to 50%. These results suggest that the main limitations in calibration approaches arise from the heterogeneity of certain standards (*e.g.*, ECRM, BPLM) and from mismatched concentration ranges between standards and samples, rather than from the calibration model itself. Thus, while one-point calibration with a homogeneous, well-characterized standard can yield accurate results under suitable conditions, multi-point calibration remains advantageous for maintaining robustness across a broader range of analytes, sample types and compensating for potential heterogeneities in the standard materials.

Although laser spot sizes of 5×5 and $10 \times 10\ \mu m^2$ (square masks) were tested and yielded good linearity for major elements such as Ba, Mn, Sr, and Pb, the reduced sensitivity at smaller spot sizes led to higher limits of detection (LODs) and

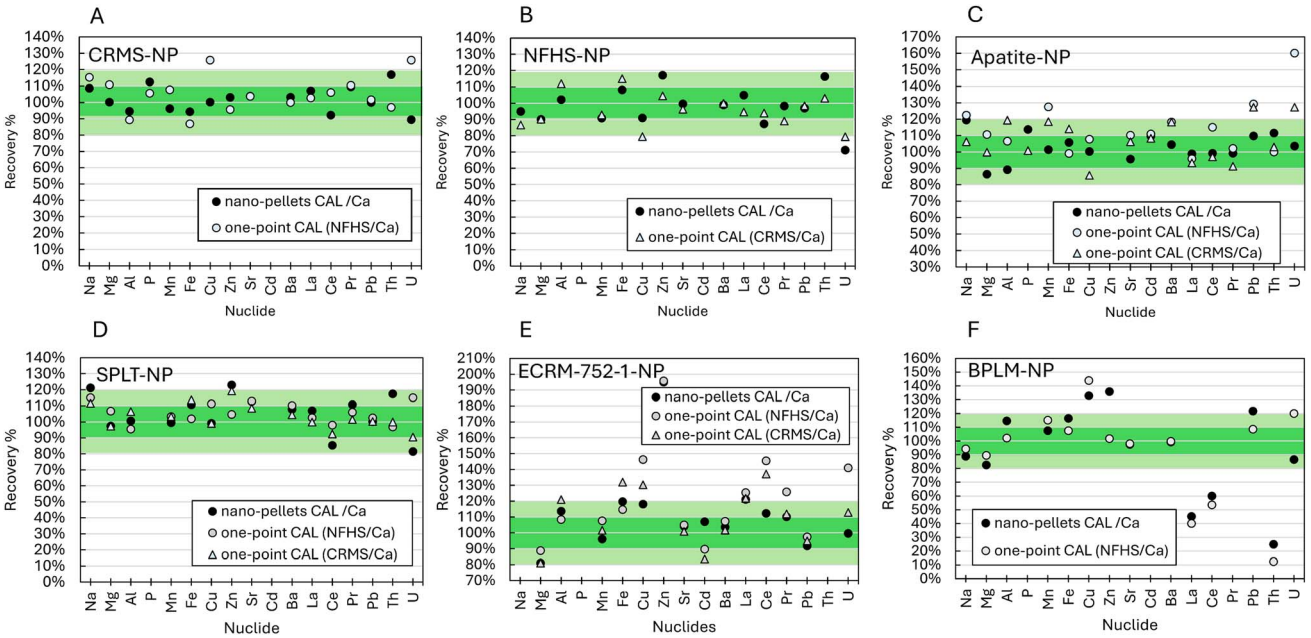

Fig. 6 Comparison of elemental recoveries – (determined value/reference value) × 100% – for target elements in different nano-pellets: (A) CRMS-NP, (B) NFHS-2-NP, (C) Apatite-NP, (D) SPLT-NP, (E) ECRM-752-1-NP, and (F) BPLM-NP. Recoveries are shown for calibrations performed using either the $N-1$ nano-pellet method or one-point calibration (using NFHS-2-NP or CRMS-NP). Shading indicates deviation ranges from the reference value (dark and light green correspond to ±10% and ±20%, respectively).

quantification (LOQs) in the μg g^{-1}-range (Table S2), hindering the monitoring of trace elements (sub- μg g^{-1} levels), especially in the low-mass range (due to the inherent lower sensitivity exhibited by TOF-based instrumentation). Nevertheless, Fig. 7 shows that for major and minor elements (above μg g^{-1} levels) the bias from the reference value remained <10% (darker green) for most of the elements (*i.e.*, Na, Mg, Al, Mn, Fe, Sr and Ba), or <20% (light green) for some (*i.e.*, Cu and Pb) even when decreasing the spot size to 5 × 5 μm^2. These results confirm that while smaller spot sizes reduce the overall sensitivity, especially critical when working with ICP-TOF-MS instrumentation, the micro-homogeneity of the nano-pellets is sufficient to provide reliable and accurate data for minor (particularly in the high-mass range) and major elements, though a full elemental overview is restricted under such conditions (*e.g.*, for Th or U, which were present at sub-ppm levels, the recoveries were less than 80% when using a 10 × 10 or 5 × 5 μm^2 laser beam).

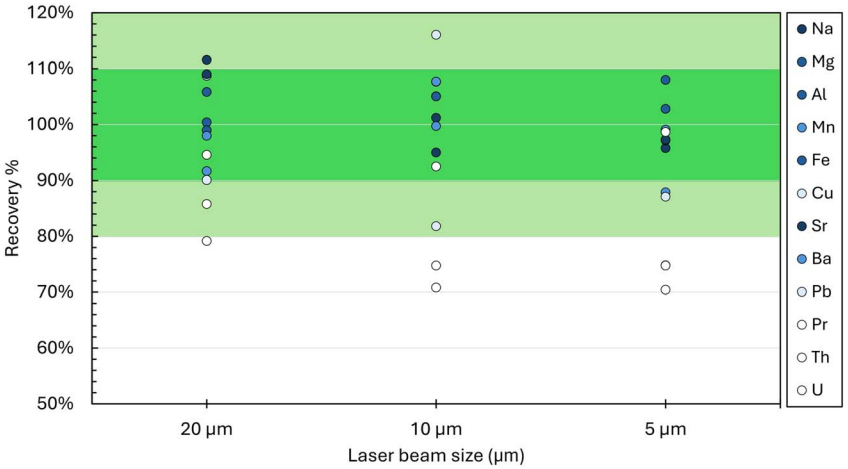

Fig. 7 Comparison of recoveries obtained using different laser beam sizes (20 μm × 20 μm, 10 μm × 10 μm, and 5 μm × 5 μm) for major, minor, and trace elements in NFHS-2-NP. The intensity of the data point colour reflects the concentration levels: from highest (Na, Sr ≈ 1000 ppm) to sub-ppm levels; (Na, Sr) > (Mg, Al, Fe) > (Mn, Ba) > (Cu, Pb) > (Pt, Th, U).

Case study: quantitative multi-elemental mapping of $CaCO_3$ samples

In this section, quantitative multi-elemental mapping of two types of $CaCO_3$-based biological samples—(1) fish otoliths and (2) bivalve shells—are presented. Data processing for these samples relied on the combined use of nano-pellets as matrix-matched standards for external calibration and Ca as an internal standard for correction of differences in the ablation yield. Both sample types are of particular interest in sclerochronological studies, as archives for short-term climate reconstruction, for extracting (paleo)biological information, in the context of fisheries studies and for reconstructing environmental histories.[46–48] To investigate the fine microstructural features of these materials, high spatial resolution is essential. While a detailed interpretation of the biological meaning of the data obtained is beyond the scope of this paper, relevant observations based on the case studies presented will be discussed briefly.

Otolith samples. Two otoliths from Atlantic cod (*Gadus morhua*), collected from two different waterbodies in Western Norway—Hardangerfjorden and Store Lungegårdsvannet (details provided in the Experimental section)—were quantitatively mapped using the LA-ICP-TOF-MS methodology developed. This method enabled quasi-simultaneous monitoring of nearly the entire elemental mass spectrum for every pixel, at a pixel acquisition rate of 50 pixels per second and with a lateral resolution of 20 μm (parameters summarized in Table 1). In this way, it was possible to distinguish growth rings, which exhibit considerable variation in thickness depending on the region of the otolith, being thinner near the core and thicker toward the edges. Also, when tracking along the vertical axis, the rings of the specimen appear more merged and were more difficult to distinguish individually compared to the horizontal view, as is displayed by the quantitative strontium (Sr) distribution shown in Fig. 8C.

The data processing workflow for generating quantitative elemental maps involved: (1) selection of the qualitative map of

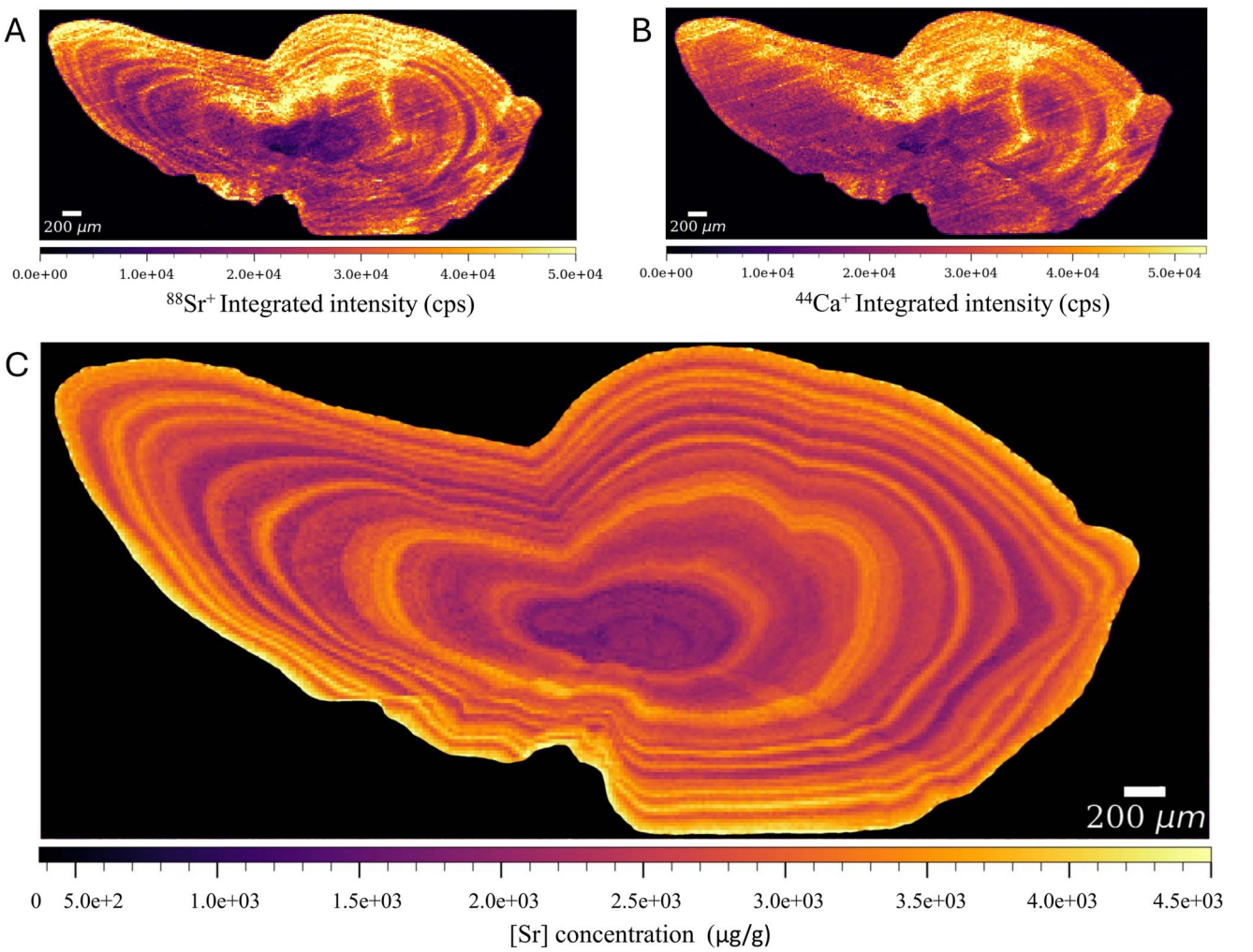

Fig. 8 LA-ICP-TOF-MS elemental maps obtained for the otolith from cod caught in the Store Lungegårdsvannet, Norway. (A) qualitative $^{88}Sr^+$ map, (B) qualitative $^{44}Ca^+$ map used for normalization and (C) quantitative map displaying the Sr distribution after Ca normalization and using the nano-pellets as external standards.

the nuclide of interest (*e.g.*, $^{88}Sr^{+}$) and of the internal standard ($^{44}Ca^{+}$) (Fig. 8A and B, respectively); (2) normalization of the target element's signal intensity at each pixel to that for $^{44}Ca^{+}$ to account for differences in ablation yield; (3) conversion of the normalized qualitative map into a quantitative one using matrix-matched external calibration against the nano-pellets ($n = 3$ lines per nano-pellet) and assuming a concentration of Ca of 40%.

Sr is typically used as a proxy for fish age. The distribution of Sr in the otolith displays concentric bands interpreted as chronological markers, as can be seen in the quantitative Sr map in Fig. 8C. However, it is also studied as a proxy for reconstructing environmental histories such as habitat shifts and waterbody changes.[48,49] In fact, Sr incorporation in otoliths reflects the ambient water chemistry—mainly salinity and temperature variations.[50,51] While these patterns may capture seasonal or episodic events, high lateral resolution mapping can reveal more Sr bands than actual annual growth increments. In this case, 15–17 Sr bands were identified in an otolith originating from a 6 year old fish, highlighting the enhanced time resolution offered by spatially resolved LA-ICP-TOF-MS mapping.[2] When examining the Mn distribution (Fig. S4A), it is still possible to distinguish an enrichment in the core regions corresponding to juvenile life (Mn concentration close to the LOQ of the method). Elevated Mn/Ca ratios were described to be related with hypoxic conditions (*i.e.*, reduced oxygen levels) typically in estuaries or sediment-rich areas.[51–54] The combination of high Mn concentration with low Sr levels in the rings near to the core suggests a juvenile phase where the animal was exposed to low oxygen (high concentration of Mn) and low salinity (low concentration rings of Sr) water environments like hypoxic bottom waters or estuaries. Peaks in Mn can also indicate metabolic activity or stress during key life events (*e.g.*, hatching, settlement).[48] The findings were compared to those for a second otolith from a cod sampled in the same waterbody (Lungegårdsvannet) that shows the same patterns: highly defined layers are observed based on the Sr distribution along the entire life of the fish, while Mn layers (higher Mn exposure) overlapping with low Sr concentration layers are only seen for early-life periods (Fig. S4B and C, respectively).

Notably, the diagonal lines—likely polishing artifacts—observed in the elemental maps of $^{88}Sr^{+}$ (Fig. 8A) and $^{44}Ca^{+}$ (Fig. 8B) are no longer visible after normalization (Fig. 8C). This demonstrates the effectiveness of IS normalization in correcting not only for matrix-related ablation yield variations (*e.g.*, due to crystallization or porosity) or instrumental drifts, but also for surface artifacts introduced during sample preparation.

For the other otolith from the cod caught in the Hardanger fjord in Norway, the Mn distribution was not revealed, but in the juvenile lines, an enrichment in Ba (Fig. 9B) coinciding with low-concentration rings of Sr (Fig. 9A) was observed. Ba is typically used as marker of specific habitat transitions.[50] While a high concentration of Sr is related to high salinity, a high concentration of Ba corresponds to low salinity environments (*i.e.*, fresh waters).[48] The co-localization of a low Sr and a high Ba concentration in the early growth rings suggests a juvenile phase where the cod inhabited shallower or more brackish environments (low salinity environments). A later migration to deeper, more saline waters (no Ba exposure) for foraging could explain the corresponding changes in element ratios recorded in the otolith. Taken together, these data underscore the value of quasi-simultaneous quantitative multi-elemental mapping in enhancing the interpretation of otolith chemistry covering the fish's lifespan. While strontium (Sr) alone may not reliably

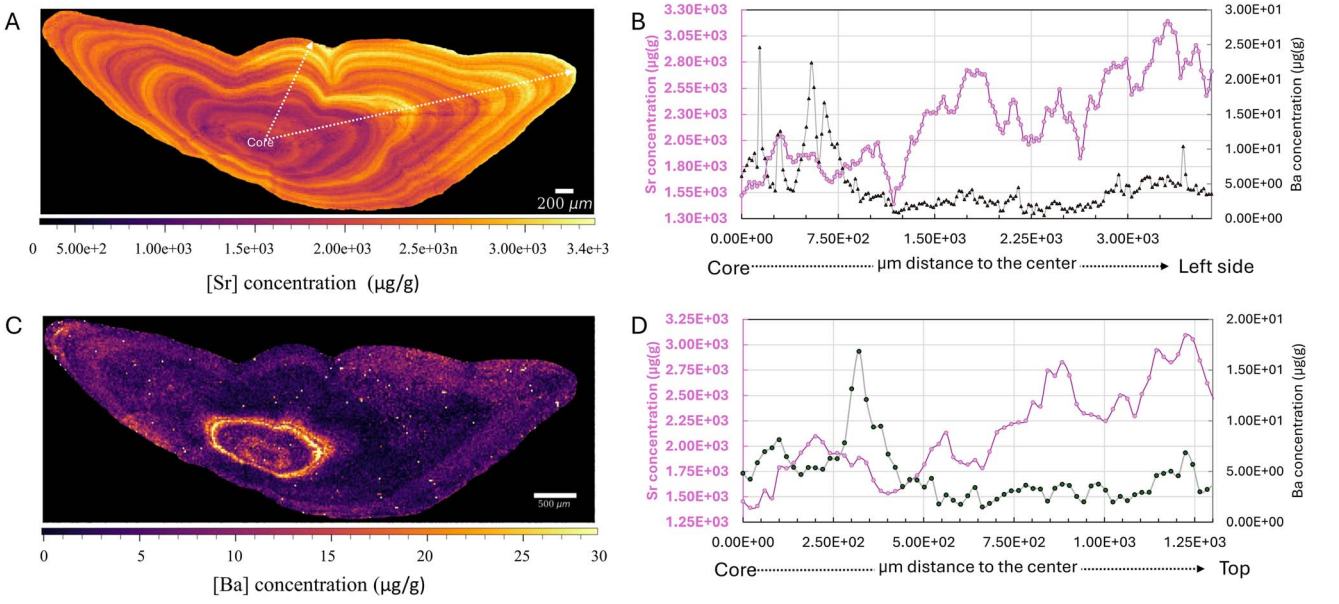

Fig. 9 Quantitative elemental maps for (A) Sr and (C) Ba for an otolith from a cod fish collected in the Hardanger fjord. Lines displaying a higher concentration of Ba are shown in the early growth rings, corresponding to lower concentrations of Sr. (B) and (D) show the 1-D line scan from core to left and core to top, respectively, with the pattern extracted from the quantitative multielemental map using HDIP software, following the lines marked in (A) by the two arrows.

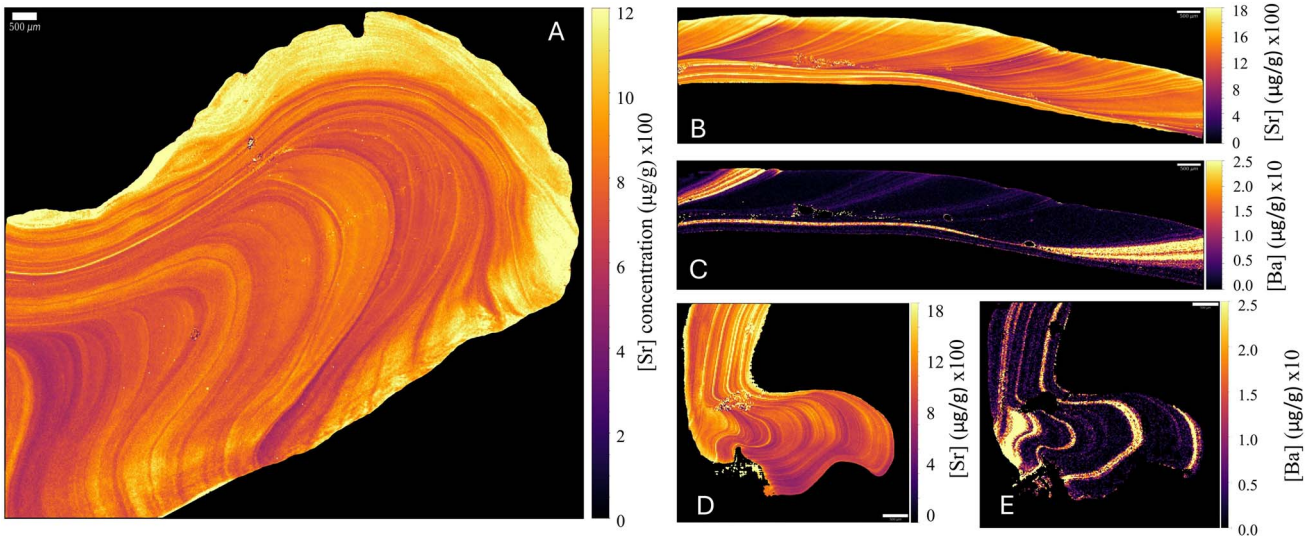

Fig. 10 Quantitative maps for Sr and Ba in two different bivalve shell types: (A) Sr distribution in oyster shell and (B) the Sr and (C) the Ba distribution in the upper part of the dorsoventral section along the axis of maximum growth and (D) the Sr and (E) the Ba distribution in the hinge area of the clam shell. The scale bar in all maps indicates 500 µm.

indicate chronological age, integrating multiple elemental ring distributions (*i.e.* Mn or Ba) enables a more nuanced reconstruction of the fish's environmental history. Noted that, fully interpreting the readings of each otolith and tracking the corresponding fish's life history requires extensive analysis, which is beyond the scope of this work.

Traditional 1D-analysis (line scanning) was compared to 2D-elemental mapping in all cases to emphasize the advantages of 2D-mapping in sclerochronological studies. Although a well-chosen 1D transect (*e.g.*, core-to-edge along the longest growth axis) can capture chronological information, it may not always represent the full spatial variability of elemental incorporation. Recent work by de Pontual *et al.*[55] demonstrated that otoliths can exhibit subtle asymmetries and heterogeneous distributions of certain elements, underscoring the limitations of relying solely on single transects. Our results are consistent with this view. As shown in Fig. 9B and C, the layer patterns for Sr and Ba differ depending on the direction of the line scan—whether from the core to the left (Fig. 9B), or from the core to the top (Fig. 9C) of the otolith. Notably, scans from the centre (juvenile layers) to the top show a loss of resolution, failing to capture the fine scale elemental distribution. In addition, as can be observed from the 2D-map (Fig. 9A and C), the layer arrangement on the left & right sides is not perfectly symmetrical. Consequently, 1D analysis can yield different patterns depending on scan orientation, potentially leading to misinterpretation of elemental (Fig. S5). By contrast, 2D-mapping provides a comprehensive view of the otolith structure, allowing potential spatial heterogeneities to be identified and interpreted more reliably.

To validate the quantitative results obtained *via* LA-ICP-TOF-MS mapping, a complementary bulk analysis was performed. From each fish, two otoliths were collected. One was embedded in epoxy resin for direct solid sampling by laser ablation, while the second was acid-digested and used for validation through conventional solution ICP-MS, as described in the Experimental Section of the SI. The results were in the same range as the values obtained by solid sampling for Sr, Ba and Mn (Table S4).

Bivalve shells. Bivalve shells, which are common archives for short-term climate reconstructions, were mapped using the same method and workflow as used for otolith analysis. The quantitative distribution of target elements (Sr and Ba) was documented across different regions of oyster (*Crassostrea gigas*; Fig. 10A) and ocean quahog shell samples (*Arctica islandica*; Fig. 10A–E). The Sr/Ca and Ba/Ca ratios in *C. gigas* (~400–1200 µg g^{-1} for Sr/Ca and ~0–25 µg g^{-1} for Ba/Ca)[56,57] and *A. islandica* (~400–1800 µg g^{-1}, and ~0–25 µg g^{-1}, for Ba/Ca) correspond to previous measurement results for these concentration ratios in the same species[58,59] demonstrating the accuracy of the LA-ICP-TOF-MS results on mollusc shell carbonate.

Notably, the ability to visualize strontium (Sr) growth lines within the shells allows for sub-annual, even monthly, climate reconstruction, highlighting the method's value in paleoclimate studies.[26,60] In this context, the Sr distribution shows rings with higher and lower concentration than can used as proxy for environmental conditions. The observation that these Sr concentration bands are continuous throughout the oyster hinge region (Fig. 10A) is of particular interest. The shell of *C. gigas* consists of alternating layers of the foliated calcite microstructure interspersed with lenses of the more porous chalky calcite microstructure, which often exhibit marked variations in chemical composition, complicating the observation of isochronous growth structures in the shells.[44,56] In the *A. Islandica* shells, localized enrichments of barium (Ba) were observed in specific growth bands both in the outer and inner shell layers of the ventral margin (Fig. 10C) and in corresponding growth bands in the shell hinge (Fig. 10E). These likely correspond to seasonal

phytoplankton bloom events in spring and/or autumn, in accordance with observations in the literature.[44] Clear seasonal banding in Sr/Ca observed in *A. islandica* (Fig. 10C and E) corroborates the timing of these Ba/Ca peaks in this specimen. An important observation in these mollusc maps is that the concentration of Sr relative to Ca is not uniform in contemporary portions of the shell (see Fig. 10A for *C. gigas* and Fig. 10B for *A. islandica*). This corroborates previous studies by Freitas *et al.*[61] who demonstrated such heterogeneity and like for the otoliths, this highlights the value of 2D-mapping for the interpretation of trace element profiles in mollusc shell material in terms of climate and environmental change.

Conclusions

The introduction of nanoparticulate pressed powder pellets has significantly enhanced the accuracy and precision attainable in quantitative LA-ICP-MS analysis of biogenic carbonates. Their higher micro-homogeneity owing to their smaller grain size permits higher reproducibility and accuracy in quantitative 2D-mapping at high spatial resolution. These findings underline the advantage of using matrix-matched nano-pellets. Unlike silicate glass reference materials such as NIST SRM 610, nano-pellets offer better matrix compatibility, resulting in lower quantification uncertainties. The use of Ca as an internal standard proved crucial not only for correcting for ablation yield differences between dissimilar matrices (*e.g.*, NIST glass *vs.* carbonate) but also for improving quantification among the different carbonate samples, which may exhibit slight but impactful matrix variations (*e.g.*, different crystallization or porosity) and for eliminating the effect of surface artifacts on the samples.

The micro-homogeneity assessments showed differences among set of the nano-pellets studied. While NFHS-2-NP, CRMS-NP, and Apatite-NP nano-pellets exhibited the highest micro-homogeneity for nearly all elements, higher RSDs and consequently poorer elemental recoveries were found for BAM-RS3-NP and BPLM-NP. It was noted that sub-μg g^{-1} elemental concentrations in the nano-pellets yielded higher RSDs. Additionally, when decreasing laser beam sizes to reach very high lateral resolution (down to 5 × 5 μm^2), LODs and LOQs deteriorated, hampering detection and quantification of trace elements at concentrations below sub-μg g^{-1}, as well as increasing uncertainties for elements close to the LOD. This reduction in sensitivity associated with the use of a smaller laser beam spot and the inherently lower sensitivity of ICP-TOF-MS instrumentation compared to quadrupole-based systems jeopardize the detection of some minor and trace elements (often in the low μg g^{-1} or even sub-μg g^{-1} range). Nevertheless, the loss of sensitivity at ultrahigh lateral resolution could in principle be compensated for by increasing both the number of laser shots per pixel (*i.e.*, using a dosage >1) and the repetition rate accordingly. While this approach could boost signal intensity, it also exponentially increases the number of required laser pulses and introduces potential challenges with detector saturation. Therefore, dosage >1 approaches may be better suited for specific regions of interest (ROIs) where very high spatial detail is required.

Overall, this quantitative multi-elemental LA-ICP-TOF-MS 2D elemental mapping approach was successfully applied to two types of biogenic carbonate samples: otoliths and bivalve shells. This methodology enabled the quantitative visualization of growth bands and internal structures, allowing distinction of seasonal and sub-seasonal growth patterns. By combining Sr and Mn maps or Sr and Ba maps, the 2D reconstructions provide additional spatial context beyond that obtained from 1D transects, supporting a more robust interpretation of carbonate archives for tracking historical events within an animal's lifespan. While Sr reflects seasonal-scale environmental variations in both archives, Mn and Ba serve as sensitive indicators of specific habitat conditions such as water oxygenation and phytoplankton blooms. Together, these tracers underline the utility of biogenic samples such as otoliths and bivalve shells as chronological environmental archives. Furthermore, comparison of 2D-maps with traditional 1D (line scanning) analyses revealed that, while 1D transects along the main growth axis can capture temporal Sr and Ba patterns, they may not consistently reflect finer-scale heterogeneities or asymmetries that occur orthogonal to the line scanning direction. This highlights the need for caution when interpreting 1D profiles and when assuming homogeneity of elemental patterns in isochronous parts of biominerals, since non-symmetrical layer structures and chemical variability within contemporary growth layers can occur. In contrast, 2D-mapping provides a more comprehensive and spatially representative view, which is essential for robust sclerochronological and environmental reconstructions.

Author contributions

Ana Lores-Padin: data curation, formal analysis, methodology, conceptualization, validation, visualization, writing – original draft. Thibaut Van Acker: conceptualization, validation, methodology, visualization, writing – review and editing. Niels J. de Winter: conceptualization, validation, resources, writing – review and editing. Martin Wiech: conceptualization, resources, writing – review and editing. Simon Nordstad: resources, writing – review and editing. Yannic Hallier: resources, writing – review and editing. Fank Vanhaecke: conceptualization, funding acquisition, project administration, supervision, visualization, writing – review and editing.

Conflicts of interest

S. N. is owner of the company myStandards. Y. H. works at myStandards. The company myStandards has provided the UGent-A&MS research group with the nano-pellet standards at no cost. The research units involved received no other financial support from myStandards for this work. A. L. P., T. V. A. and F. V. conduct research at a research unit that has licensed intellectual property to Teledyne Photon Machines.

Data availability

Data will be made available upon request.

Supplementary information is available. See DOI: https://doi.org/10.1039/d5ja00280j.

Acknowledgements

A. L. P. and T. V. A. thank the Research Foundation Flanders for support under the form of their junior postdoctoral research fellowships (FWO 1276325N and 1218423N, respectively). N. J. W. acknowledges support from the Netherlands Research Council (NWO) for a personal VENI research fellowship (VI.Veni.222.354) and from the Flemish Research Council (FWO Science Prize Climate Research 2024). We would like to thank the following persons at the Institute of Marine Research, Norway for their contributions: Kai Kristoffer Lie for providing the otoliths of the Atlantic cod sampled in Hardanger, Åse Husebø for embedding and cutting the otoliths, and Erlend Langhelle for age determination of the Atlantic cod based on the otolith rings.

References

1 J. Vellekoop, D. Vanhove, I. Jelu, P. Claeys, L. C. Ivany, N. J. de Winter, R. P. Speijer and E. Steurbaut, *Palaeogeogr., Palaeoclimatol., Palaeoecol.*, 2025, **659**, 112627.
2 H. Tabouret, G. Bareille, F. Claverie, C. Pécheyran, P. Prouzet and O. F. X. Donard, *Mar. Environ. Res.*, 2010, **70**, 35–45.
3 D. Chew, K. Drost, J. H. Marsh and J. A. Petrus, *Chem. Geol.*, 2021, **559**, 119917.
4 Y. S. Liu, Z. C. Hu, M. Li and S. Gao, *Chin. Sci. Bull.*, 2013, **58**, 3863–3878.
5 A. Limbeck, P. Galler, M. Bonta, G. Bauer, W. Nischkauer and F. Vanhaecke, *Anal. Bioanal. Chem.*, 2015, **407**, 6593–6617.
6 S. Marali, B. R. Schöne, R. Mertz-Kraus, S. M. Griffin, A. D. Wanamaker, P. G. Butler, H. A. Holland and K. P. Jochum, *Palaeogeogr., Palaeoclimatol., Palaeoecol.*, 2017, **484**, 109–128.
7 H. A. O. Wang, D. Grolimund, C. Giesen, C. N. Borca, J. R. H. Shaw-Stewart, B. Bodenmiller and D. Günther, *Anal. Chem.*, 2013, **85**, 10107–10116.
8 S. J. M. Van Malderen, T. Van Acker and F. Vanhaecke, *Anal. Chem.*, 2020, **92**, 5756–5764.
9 T. Van Acker, S. J. M. Van Malderen, T. Van Helden, C. Stremtan, M. Šala, J. T. Van Elteren and F. Vanhaecke, *J. Anal. At. Spectrom.*, 2021, **36**, 1201–1209.
10 A. Gundlach-Graham and D. Günther, *Anal. Bioanal. Chem.*, 2016, **408**, 2687–2695.
11 I. Basabe-Mendizabal, R. Maeda, S. Goderis, F. Vanhaecke and T. Van Acker, *Anal. Chem.*, 2025, **97**, 6481–6488.
12 B. Hattendorf, C. Latkoczy and D. Günther, *Anal. Chem.*, 2003, **75**, 341–347.
13 K. P. Jochum, D. Scholz, B. Stoll, U. Weis, S. A. Wilson, Q. Yang, A. Schwalb, N. Börner, D. E. Jacob and M. O. Andreae, *Chem. Geol.*, 2012, **318–319**, 31–44.
14 T. E. Jeffries, S. E. Jackson and H. P. Longerich, *J. Anal. At. Spectrom.*, 1998, **13**, 935–940.
15 M. Guillong, I. Horn and D. Günther, *J. Anal. At. Spectrom.*, 2003, **18**, 1224–1230.
16 W. Müller and J. Fietzke, *Elements*, 2016, **12**, 329–334.
17 N. Miliszkiewicz, S. Walas and A. Tobiasz, *R. Soc. Chem.*, 2015, **30**, 327–338.
18 K. P. Jochum, D. Garbe-Schönberg, M. Veter, B. Stoll, U. Weis, M. Weber, F. Lugli, A. Jentzen, R. Schiebel, J. A. Wassenburg, D. E. Jacob and G. H. Haug, *Geostand. Geoanal. Res.*, 2019, **43**, 595–609.
19 N. Sekhon, A. Gao, S. Mallick, J. W. Partin, M. B. Cardenas and D. E. Ibarra, *Rapid Commun. Mass Spectrom.*, 2025, **39**, 9983.
20 J. A. Thompson, J. M. Thompson, K. Goemann, E. Lounejeva, D. R. Cooke and L. Danyushevsky, *Geostand. Geoanal. Res.*, 2022, **46**, 97–115.
21 K. P. Jochum, U. Weis, B. Stoll, D. Kuzmin, Q. Yang, I. Raczek, D. E. Jacob, A. Stracke, K. Birbaum, D. A. Frick, D. Günther and J. Enzweiler, *Geostand. Geoanal. Res.*, 2011, **35**, 397–429.
22 I. Kroslakova and D. Günther, *J. Anal. At. Spectrom.*, 2007, **22**, 51–62.
23 W. T. Perkins, R. Fuge and N. J. G. Pearce, *J. Anal. At. Spectrom.*, 1991, **6**, 445–449.
24 S. J. Fallon, M. T. Mcculloch, R. Van Woesik and D. J. Sinclair, *Corals at Their Latitudinal Limits: Laser Ablation Trace Element Systematics in Porites from Shirigai Bay,* Japan, 1999, vol. 172.
25 N. M. V. R. Bellotto, *Fresenius. J. Anal. Chem.*, 2000, **367**, 365–640.
26 A. Barats, C. Pécheyran, D. Amouroux, S. Dubascoux, L. Chauvaud and O. F. X. Donard, *Anal. Bioanal. Chem.*, 2007, **387**, 1131–1140.
27 K. Ulens, L. Moens, R. Dams, S. Van Winckel and L. Vandevelde, *Study of Element Distributions in Weathered Marble Crusts Using Laser Ablation Inductively Coupled Plasma Mass Spectrometry*, 1994, vol. 9.
28 J. Pisonero, E. Avigliano, C. Soto-Gancedo, A. Méndez-Vicente, C. Méndez-López, J. Orejas and N. Bordel, *J. Anal. At. Spectrom.*, 2024, **39**, 601–609.
29 A. V. Lazartigues, P. Sirois and D. Savard, *Geostand. Geoanal. Res.*, 2013, **38**, 225–240.
30 D. Garbe-Schönberg and S. Müller, *J. Anal. At. Spectrom.*, 2014, **29**, 990–1000.
31 C. D. Standish, J. A. Milton, T. M. Page, R. M. Brown, D. Douglas, B. Paul, L. Schlatt and G. L. Foster, *Chem. Geol.*, 2024, **670**, 122438.
32 S. R. Durham, D. P. Gillikin, D. H. Goodwin and G. P. Dietl, *Palaeogeogr., Palaeoclimatol., Palaeoecol.*, 2017, **485**, 201–209.
33 K. E. Limburg and M. Elfman, *J. Fish Biol.*, 2017, **90**, 480–491.
34 K. E. Limburg, R. Huang and D. H. Bilderback, *X-Ray Spectrom.*, 2007, **36**, 336–342.
35 N. J. de Winter and P. Claeys, *Sedimentology*, 2017, **64**, 231–251.
36 N. J. De Winter, M. Sinnesael, C. Makarona, S. Vansteenberge and P. Claeys, *J. Anal. At. Spectrom.*, 2017, **32**, 1211–1223.
37 K. Thorn, R. M. Cerrato and M. L. Rivers, Elemental Distributions in Marine Bivalve Shells as Measured by

Synchrotron X-Ray Elemental Distributions in Marine Bivalve Shells as Measured by Synchrotron X-Ray Fluorescence, *Biol. Bull.*, 1995, **188**, 57–67.
38 Y. Tamenori and T. Yoshimura, *Geochim. Cosmochim. Acta*, 2018, **237**, 357–369.
39 L. Hendriks, A. Gundlach-Graham, B. Hattendorf and D. Günther, *J. Anal. At. Spectrom.*, 2017, **32**, 548–561.
40 W. Boer, S. Nordstad, M. Weber, R. Mertz-Kraus, B. Hönisch, J. Bijma, M. Raitzsch, D. Wilhelms-Dick, G. L. Foster, H. Goring-Harford, D. Nürnberg, F. Hauff, H. Kuhnert, F. Lugli, H. Spero, M. Rosner, P. van Gaever, L. J. de Nooijer and G. J. Reichart, *Geostand. Geoanal. Res.*, 2022, **46**, 411–432.
41 my-Standards, *myStandards-nano-pellets*, **https://www.my-standards.com/standards/carbonate-standards**, accessed 20 May 2025.
42 K. P. Jochum, U. Nohl, K. Herwig, E. Lammel, B. Stoll and A. W. Hofmann, *GeoReM: A New Geochemical Database for Reference Materials and Isotopic Standards*, **https://georem.mpch-mainz.gwdg.de/CiteGeorem.html**, accessed 24 June 2025.
43 D. Hippler, R. Witbaard, H. M. van Aken, D. Buhl and A. Immenhauser, *Palaeogeogr., Palaeoclimatol., Palaeoecol.*, 2013, **373**, 75–87.
44 N. J. de Winter, L. K. Dämmer, M. Falkenroth, G. J. Reichart, S. Moretti, A. Martínez-García, N. Höche, B. R. Schöne, K. Rodiouchkina, S. Goderis, F. Vanhaecke, S. M. van Leeuwen and M. Ziegler, *Geochim. Cosmochim. Acta*, 2021, **308**, 326–352.
45 M. Burger, L. Hendriks, J. Kaeslin, A. Gundlach-Graham, B. Hattendorf and D. Günther, *J. Anal. At. Spectrom.*, 2019, **34**, 135–146.
46 D. K. Moss, L. C. Ivany and D. S. Jones, *Paleobiology*, 2021, **47**, 551–573.
47 D. S. Jones, *Am. Sci.*, 1983, 384391.
48 P. Reis-Santos, B. M. Gillanders, A. M. Sturrock, C. Izzo, D. S. Oxman, J. A. Lueders-Dumont, K. Hüssy, S. E. Tanner, T. Rogers, Z. A. Doubleday, A. H. Andrews, C. Trueman, D. Brophy, J. D. Thiem, L. J. Baumgartner, M. Willmes, M. T. Chung, P. Charapata, R. C. Johnson, S. Trumble, Y. Heimbrand, K. E. Limburg and B. D. Walther, *Rev. Fish Biol. Fish.*, 2023, **33**, 411–449.
49 H. Tabouret, G. Bareille, F. Claverie, C. Pécheyran, P. Prouzet and O. F. X. Donard, *Mar. Environ. Res.*, 2010, **70**, 35–45.
50 C. Gauthier, J. A. D. Fisher, D. Robert and P. Sirois, *ICES J. Mar. Sci.*, 2024, **81**, 1221–1233.
51 P. D. Collingsworth, J. J. van Tassell, J. W. Olesik and E. A. Marschall, *Can. J. Fish. Aquat. Sci.*, 2010, **67**, 1187–1196.
52 J. Kemp, S. E. Swearer, G. P. Jenkins and S. Robertson, *Can. J. Fish. Aquat. Sci.*, 2011, **68**, 1732–1743.
53 G. D'Avignon and G. A. Rose, *Fish. Res.*, 2013, **147**, 1–9.
54 M. M. Ranaldi and M. M. Gagnon, *Comp. Biochem. Physiol. C Comp. Pharmacol. Toxicol.*, 2010, **152**, 248–255.
55 H. de Pontual, K. M. MacKenzie, H. Tabouret, F. Daverat, K. Mahé, C. Pecheyran and K. Hüssy, *J. Fish. Biol.*, 2024, **104**, 20–33.
56 C. V. Ullmann, F. Böhm, R. E. M. Rickaby, U. Wiechert and C. Korte, *Geochem., Geophys., Geosyst.*, 2013, **14**, 4109–4120.
57 D. H. Goodwin, D. P. Gillikin and P. D. Roopnarine, *Palaeogeogr., Palaeoclimatol., Palaeoecol.*, 2013, **373**, 88–97.
58 B. R. Schöne, Z. Zhang, P. Radermacher, J. Thébault, D. E. Jacob, E. V. Nunn and A. F. Maurer, *Palaeogeogr., Palaeoclimatol., Palaeoecol.*, 2011, **302**, 52–64.
59 B. R. Schöne, P. Radermacher, Z. Zhang and D. E. Jacob, *Palaeogeogr., Palaeoclimatol., Palaeoecol.*, 2013, **373**, 50–59.
60 S. V. Popov, *Paleontol. J.*, 2014, **48**, 1519–1531.
61 P. S. Freitas, L. J. Clarke, H. Kennedy and C. A. Richardson, *Ion Microprobe Assessment of the Heterogeneity of Mg/Ca, Sr/Ca and Mn/Ca Ratios in Pecten maximus and Mytilus edulis (Bivalvia) Shell Calcite Precipitated at Constant Temperature*, 2009, vol. 6.